**TECHNISCHE
UNIVERSITÄT
WIEN**

Vienna University of Technology

DIPLOMARBEIT

Overcoming Blinking Artifacts in Nanocluster Detection Using Two-Color Single-Molecule Microscopy

ausgeführt am

Institut für Angewandte Physik

der Technischen Universität Wien

unter der Anleitung von

Univ.-Prof. Gerhard J. Schütz

und

Dipl.-Ing. Andreas M. Arnold

mit Mitwirkung von

Florian Baumgart, PhD

durch

Magdalena Schneider, BSc

Matrikelnummer: 11227037

Wien, am 22. März 2018

Kurzfassung

Die Entwicklung von Einzelmolekülmikroskopiemethoden im letzten Jahrzehnt hat die Untersuchung von Proteinen in der Zellmembran mit einer bisher unerreichten Auflösung von bis zu 10 nm ermöglicht. Eine Vielzahl nachfolgender Experimente führte zu der Annahme, dass ein erheblicher Anteil aller Proteine in der Zellmembran in Gruppierungen (üblicherweise bezeichnet als Cluster) von einer Größenordung unterhalb der Diffraktionsgrenze angeordnet ist. Es wird vermutet, dass diese Nanocluster eine wichtige Rolle in der zellulären Kommunikation spielen. Die Erkenntnis, dass fast alle Fluorophore ein komplexes Blinkverhalten inklusive lang andauernder Dunkelzustände aufweisen, ließ jedoch Zweifel über die tatsächliche Existenz von Nanoclustern aufkommen. Denn das Blinkverhalten von Fluorophoren führt zur wiederholten Detektion von ein und demselben Molekül. Dies resultiert in geclusterten Lokalisationen ohne zugrundeliegende echte molekulare Cluster. Verschiedene Nachbearbeitungsstrategien wurden entwickelt, um echtes molekulares Clustering von solchen Lokalisationsclustern zu unterscheiden. Diese weisen aber oft Unzulänglichkeiten auf, vor allem bei Clustern deren Größenordnung im Bereich der Lokalisierungsgenauigkeit liegt.

Die vorliegende Arbeit stellt eine neue analytische Methode vor, die mittels der Informationen aus Zweifarbeneinzelmolekülmikroskopie molekulares Clustering zuverlässig erkennt, dabei aber die falsche Detektion von Clustern aufgrund von Fluorophorblinken verhindert. Das zu untersuchende Protein wird dafür mit zwei unterschiedlichen Fluorophoren markiert, die voneinander verschiedene Emissionsspektren aufweisen. Dies erlaubt die Bestimmung von Distanzverteilungen zwischen den Lokalisationen aus beiden Farbkanälen. Echte molekulare Cluster weisen hierbei eine charakteristische Tendenz zu geringeren Distanzen auf. Vorhandene Korrelationen zwischen den Farbkanälen werden aufgelöst, indem alle Daten aus einem der Farbkanäle auf der Geometrie eines Torus verschoben werden. Dies liefert einen Ersatz für Realisierungen der Nullhypothese zufällig verteilter Moleküle auf der Zellmembran. Hierdurch wird das Durchführen statistischer Signifikanztests ohne die Notwendigkeit zusätzlicher Messdaten ermöglicht. Die Verlässlichkeit und Grenzen der Methode wurden mittels Monte Carlo Simulationen sowie Experimenten mit zufällig verteilten und geclusterten Molekülen untersucht.

Abstract

Observations using single-molecule localization microscopy have led to the belief that the majority of tested membrane proteins are organized in clusters at sizes below the diffraction limit. These nanoclusters are thought to play an important role in cellular signaling. However, concerns about the existence of nanoclusters have been fueled by the notion that virtually all fluorescent probes show complex blinking behavior including long-lived dark states. This results in localization clusters due to the repeated observation of single molecules. Existing post-processing approaches commonly struggle to reliably distinguish real molecular clustering from such blinking artifacts.

In this thesis, a novel analytical method is presented that uses information from two-color STORM experiments for reliably detecting molecular clustering while overcoming the erroneous detection of clustering due to fluorophore blinking. Targeting the same protein species with differently labeled antibodies allows for the calculation of distance distributions between localizations from both color channels. Molecular clusters exhibit a characteristic bias towards shorter distances. Applying toroidal shifts to the data breaks possible correlations between the two color channels, thus providing surrogates for realizations of the null hypothesis of randomly distributed molecules. This allows for statistical significance tests without the necessity of additional calibration. This work evaluates the limits of the method with Monte Carlo simulations and experiments on clustered and randomly distributed membrane proteins.

Acknowledgements

At this point, I want to express my thanks to all people that have supported me throughout my whole studies and in particular during my work on my diploma thesis.

First of all, I want to thank my advisor Gerhard Schütz, whose enthusiasm for scientific work and biophysics, in particular, is truly inspiring. Thanks for all the encouragement and support of my research, for all valuable comments, remarks and questions that broaden my horizon!

Special thanks to my additional supervisor Andreas Arnold and also Florian Baumgart, for being always there for answering my questions, for performing work on cell culture and experiments and for creating such an amicable working atmosphere. Thanks also for valuable inputs and remarks on the manuscript!

Besides, I would like to extend my thanks to the whole team of the biopyhsics group of TU Wien, for help, support and a pleasant time at work.

Special gratitude and thanks I owe to my parents and my whole family, for supporting me throughout my whole studies and making it possible for me to pursue all my interests.

My deepest gratitude and appreciation I want to express to Michael Innerberger, for his love and unconditional support in whatever I do.

Finally, I want to thank all my fellow students and friends that made my years of study a great experience.

Contents

Chapter 1

Introduction

The spatial distribution of proteins in the plasma membrane of cells, in particular any kind of oligomerization or clustering, is believed to be an important factor in cellular signaling. Developments of single-molecule localization microscopy (SMLM) techniques, like stochastic optical reconstruction microscopy (STORM) and photo-activated localization microscopy (PALM), achieve imaging at a resolution below the diffraction limit [1]. Thus, they allow for studying proteins in the cell membrane in unprecedented detail and detecting oligomerization and nanoclustering [2, 3, 4].

Single-molecule localization techniques rely on the stochastic activation of only a subset of fluorophores. This allows to determine the position of a single emitter with a high accuracy of typically 10–20 nm [5]. After recording and analyzing several thousands frames, all localizations are combined and result in the final image. Using SMLM-techniques, various studies have investigated the distribution of molecules in the cell membrane and commonly reported clustering at a scale between the estimated localization precision and the diffraction limit [6]. Those findings led to the believe that nanoclustering is a prevalent mechanism of plasma membrane organization. However, recent studies have raised doubts about the existence of nanoclusters by pointing to the fact that repeated observations of single fluorophores also result in clustered localizations [7, 8, 9, 10, 11]. In addition, those arguments are supported by findings that commonly used fluorescent probes exhibit long-lived dark states and may be detected several times. Simulations show that localization clusters due to repeated observation of single molecules are hard to distinguish from real molecular clusters and oligomerization (compare figure 1.1).

For overcoming these blinking artifacts, several post-processing strategies have been proposed that are supposed to account for fluorophore blinking [7, 8, 9, 11]. However, many of those techniques commonly struggle to reliably distinguish blinking artifacts from real molecular clustering. An experimental approach based on the variation of labeling density has been suggested by Baumgart et al. [12]. This approach is able to detect real molecular clustering more reliably, but has the disadvantage of being quite laborious as it requires a large number of recorded datasets.

This thesis presents a novel analytical method using information from two-color single-molecule localization experiments for overcoming the erroneous detection of clustering due to
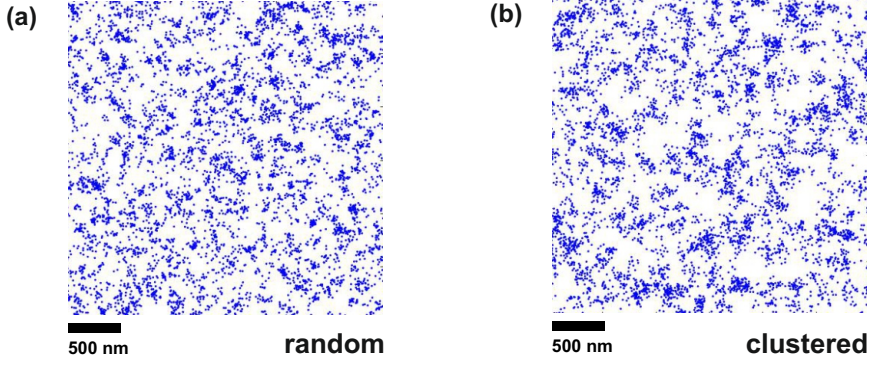
Figure 1.1: Exemplary simulated data of (a) randomly distributed and (b) clustered molecules (all molecules present as dimers) for a one-color single-molecule localization experiment. The number of simulated molecules was 150 molecules per $\mu\mathrm{m}^2$.

fluorophore blinking. Two-color single-molecule microscopy in combination with the calculation of nearest-neighbor distances has been previously used by Lopes et al. for the investigation of associations between different proteins [13]. Here, we target the same molecule of interest with differently labeled antibodies. This allows for separation of the localizations into two different color channels. Localizations arising from a single molecule will be of one color only, whereas molecules in real molecular clusters can be labeled with different types of fluorophores and hence, yield clustered localizations that show both colors as can be seen in figure 1.2. As a next step, we calculate the distances of localizations from one of the color channels to their nearest neighbor in the other channel. Applying toroidal shifts to the data of one color channel breaks possible correlations between channels, thus providing surrogates for realizations of the null hypothesis of randomly distributed molecules. Comparing the nearest-neighbor distributions of the original data to those of the shifted data allows for discriminating between localization clusters that are a result of blinking and real molecular clusters, as the latter exhibit a characteristic bias towards shorter nearest-neighbor distances before shifting.
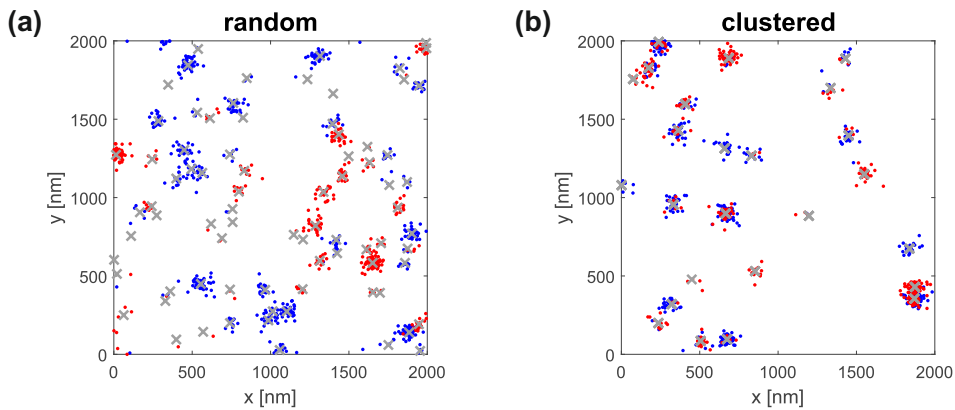

Figure 1.2: Exemplary two-color data. Simulations of (a) randomly distributed and (b) clustered molecules (all molecules present as tetramers). Labeling efficiency was 95% and label ratio 50:50. Blue and red circles represent localizations in color channel 1 and 2, respectively. Grey crosses mark the actual positions of simulated molecules.

Chapter 2

Background

Clustering on the Plasma Membrane

2.1 The Plasma Membrane

A cell is enclosed by its plasma membrane, which separates the cytosolic interior of the cell from the extracellular environment. The general structure of the cell membrane is delineated in figure 2.1. It consists of a double layer of lipids, the lipid bilayer, that is approximately 5 nm in thickness and held together primarily by hydrophobic interactions. The lipids are arranged such that their hydrophilic headgroups are on the outside of the membrane while the hydrophobic fatty acid chains face each other on the inside. The hydrophobic interior makes the bilayer nearly impermeable to water-soluble molecules. Besides lipids, the cell membrane also contains a lot of proteins that are embedded in the lipid bilayer. It is estimated that up to 30 percent of all proteins encoded in animal and human genome constitute membrane proteins that fulfill a wide range of different functions. For example, ion channels can establish ion gradients across the cell membrane that can be used to transfer ions or molecules across the membrane, transmit electrical signals, or synthesize adenosine triphosphate (ATP) used for energy storage. Other kinds of proteins, called receptors, are specialized for sensing external signals or changes in the environment, thus allowing the cell to respond to those signals in an appropriate way. [14]

A very well-known and influential model of the structure and composition of the cell membrane, the *fluid mosaic model*, was proposed by Singer and Nicolson in 1972 [15]. It states that the cell membrane is a two-dimensional fluid structure and its constituents are able to freely move around. In this model, proteins are thought to be present in the cell membrane at low concentrations only, mainly in a monomeric state and dispersed randomly. Later findings have suggested a different model of the cell membrane. Nowadays, it is generally accepted that the cell membrane is actually densely populated by proteins and very crowded [16]. Its composition and structure is quite heterogeneous. Due to interactions between lipids and proteins many molecules are found to be grouped together, often forming large functional complexes.
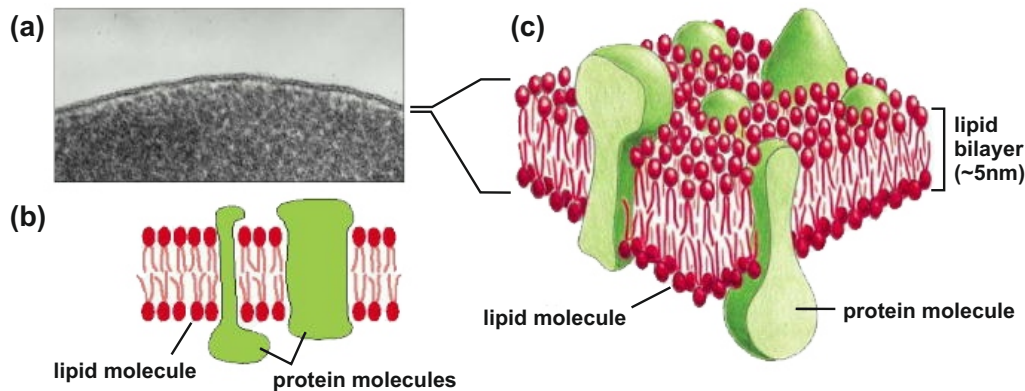
Figure 2.1: The cell membrane. **(a)** Electron microscope image of a cross section of a cell plasma membrane. **(b, c)** Sketches of the cell plasma membrane in 2D and 3D, respectively. Figure adapted from Alberts et al. [14].

2.2 Oligomerization and Nanoclustering

Interactions between proteins play a crucial role for cellular processes, especially in cellular signaling. Noncovalent bonds and forces between individual proteins may lead to the formation of oligomers. They can be formed of proteins of the same type (homooligomers) or proteins of different types (heterooligomers).

Several recent studies have reported that investigated proteins showed a heterogeneous distribution on the cell membrane and were organized in clusters at the nanoscale [6, 17, 18]. The origin of those clusters is rather unclear and often unknown. However, nanoclusters are believed to have a similar role as oligomers [19, 20, 21]. For example, they could be involved in allosteric regulation. Moreover, they offer multiple binding sites for ligands in close proximity. For multivalent ligands, this might increase the affinity for ligand-binding [22], while for monovalent ligands, the overall time of ligand-binding is prolonged due to easier rebinding of the ligand [23]. Nanoclustering has been observed for a wide range of proteins, for lipid-linked proteins as well as for transmembrane proteins. Amongst others, various glycosylphosphatidylinositol (GPI)-anchored proteins and several transmembrane proteins that play an important role in the immune system have been reported to feature nanoclustering [6].

However, the ubiquitous observation that proteins are organized in nanoclusters has been doubted recently due to findings that many used fluorescent probes show complex blinking behavior. Not all fluorophores bleach after their first detection, but undergo repeated transitions between bright and dark states. Therefore, a fluorophore might appear several times. However, the spatial coordinates assigned to the fluorophore differ slightly for each detection. This is due to restricted localization precision and other factors like residual diffusion of molecules after chemical fixation [24]. Because the fluorophore is detected at different positions, it is interpreted as multiple emitters. This overcounting leads to localization clusters that could be misinterpreted as molecular clustering.

The investigation of the blinking behavior of specific fluorescent probes has led to the find-

ings that, for example, the organic dye Alexa Fluor 647 is on average detected 5.9 ± 0.5 (mean $\pm$ standard deviation) times per fluorescent emitter [25]. The labeling of a single molecule of interest with multiple fluorophores further increases the problem of overcounting [26]. Preliminary data for the blinking behavior of the fluorescent protein PS-CFP2 and Alexa Fluor 647 bound to CD3 monoclonal antibody (clone KT3) or TCR β chain antibody (clone H57-597) were recorded in our laboratory. The experiments showed that single molecules were detected up to 15, 147 or 1572 times, respectively (compare section 4.1 and blinking statistics in the appendix A.2).

Various methods and algorithms are available to detect and quantify clustering. A few selected methods will be briefly described in the following and are illustrated in figure 2.2. One approach is to investigate the spatial distribution of localizations using Ripley's K-function [27]. This function counts the number of neighboring points within a given distance of each individual point. The resulting average number of neighboring points is then compared to the expected average under complete spatial randomness. If the pattern of interest exhibits a higher number of neighbors than expected under a random distribution, the pattern is assumed to show clustering. Ripley's-K function is usually calculated for various distances to investigate the spatial distribution of points at different scales. However, Ripley's K-function does not account for blinking artifacts.

A variant of Ripley's K-function is the pair-correlation function (PCA) that counts the number of points in rings rather than in full circles around each point. This allows for measuring the spatial association at specific scales without any bias resulting from association at smaller scales. An approach based on PCA was used by Sengupta et al. for the detection of true molecular clustering while avoiding localization clusters caused by blinking artifacts. For this, they calculated the total pair-wise correlation function that is composed of a contribution from the correlation due to multiple detection of the same molecule and a contribution from correlations due to the spatial distribution of molecules [11]. For each of the two cases of randomly distributed and clustered molecules the total pair-wise correlation function has a different form, given by equations (1) and (2) in Sengupta [11]. The distribution of molecules is indicated by a fit of the calculated pair-wise correlation function of all localizations to the respective equation. However, the method of PCA struggles if the scale of clustering is not significantly larger than the scale at which localizations from the same molecule can occur due to limited positional accuracy or residual diffusion.

Another post-processing strategy to overcome blinking artifacts and determine the true distribution of proteins on the plasma membrane of a cell was proposed by Annibale et al. They suggested to combine localizations that are in close proximity in space as well as in time and regard them as a single emitter only [7, 8, 9]. However, thresholds can be set arbitrarily and depending on their values, different scenarios of clustering are obtained. Moreover, this approach does not account for long-lived dark states and hence, cannot reliably distinguish true molecular clustering from overcounting artifacts.

An experimental approach to distinguish real molecular clusters from blinking artifacts was

presented by Baumgart et al. [12]. Variation of labeling density leads to characteristic changes in the obtained localization maps. The relative area covered by localization clusters is plotted against the normalized density of the number of localizations inside these clusters at various label densities. Deviation of the obtain curve from a simulated control curve for random distributions indicates clustering of proteins in the cell membrane. This method is able to reliably detect molecular clustering, however, it requires a large number of recorded datasets.
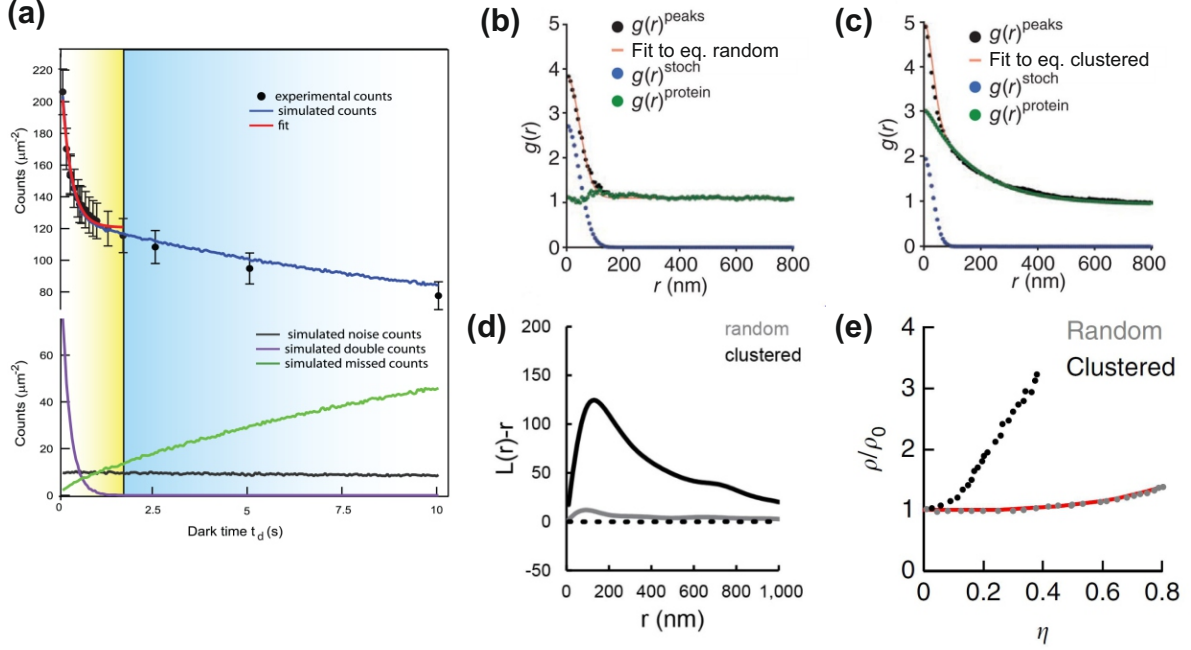
Figure 2.2: Overview of various methods for the detection of clustering. (a) Threshold of dark time by Annibale et al. [8]. Number of localizations as a function of dark time t_d, the time a molecule is allowed to be in the dark state before being identified as a different molecule.
(b, c) Pair-correlation analysis by Sengupta et al. [11]. The distribution of molecules is determined depending on whether the obtained pair-wise correlation function fits to the equation for randomly distributed molecules or the equation for clustering. (d) Ripley's K function [27]. Positive deviations of the function $L(r)-r$ from zero indicate clustering at the respective scale. (e) Variation of labeling density [12]. Relative area covered by localization clusters plotted against the normalized density of number of localizations inside the clusters at various label densities. Figures adapted from Annibale [8], Sengupta [11] and Baumgart [12].

Chapter 3

Background

Super-Resolution Microscopy

Conventional light microscopy relies on optical properties such as absorption, refraction and phase shift of a specimen for image acquisition. However, diffraction of light imposes a limit on the resolution of conventional microscopy techniques. In the last decade, several new approaches have been proposed that circumvent this diffraction barrier. Important methods include near-field scanning optical microscopy (NSOM, [28]), stimulated emission depletion microscopy (STED, [29, 30]), photoactivated localization microscopy (PALM, [31]) and stochastic optical reconstruction microscopy (STORM, [32]), among others. These super-resolution microscopy techniques allow imaging with a resolution of typically 10–20 nm. This allows for studying biological systems at a molecular level and investigate nanoscale spatial distributions and stoichiometry.

3.1 Diffraction and Resolution Limit

The interaction of an electromagnetic wave with an object leads to the spreading of the wave into the geometrical shadow of the object. This phenomenon is called diffraction and can be described theoretically by the Huygens-Fresnel principle and the interference of waves. In optical microscopy, diffraction results in a point object not being imaged as a point, but as the Airy pattern. The form of an Airy pattern is shown in figure 3.1. The intensity I of this diffraction pattern is radially symmetric and can be described by the equation

$$I(\theta) = I_0 \left(\frac{2\,J_1\big(ka\,\sin(\theta)\big)}{ka\,\sin(\theta)} \right)^2 , \tag{3.1}$$

where I_0 is the maximum intensity of the Airy disc center, θ the angle of observation, J_1 the Bessel function of the first kind of order one, $k = 2\pi/\lambda$ the angular wavenumber, and a the aperture radius. The pattern consists of a diffraction disk at the center, the 0th order diffraction spot, and is surrounded by several diffraction rings that are referred to as 1st, 2nd, 3rd, etc.,

order diffraction rings.

In 1873, Ernst Abbe found that an illuminated optical grating can be resolved if the objective lens can at least capture the 0th and 1st order diffraction maxima. This is the case if the spacing d between the lines of the grating is at least

$$d = \frac{\lambda}{2n\sin(\alpha)} = \frac{\lambda}{2\,NA}\,,\tag{3.2}$$

where λ is the wavelength of light, n the refractive index of the imaging medium, α half the aperture angle of the objective, and NA the numerical aperture of the objective. Hence, resolution can be increased by increasing the numerical aperture of the objective, or using imaging light of lower wavelength. Even under ideal conditions however, the resolution of optical microscopy is still limited to approximately 200–250 nm.

Another approach to defining resolution is the Rayleigh criterion. It states that two distinct point sources of light are resolvable if the distance d between their respective 0th order maxima is at least the radius of the central disk of the patterns, which is the distance between the 0th order maximum and the first minimum of the Airy pattern. It is given by the equation

$$d = \frac{1.22\,\lambda}{2\,NA}\,.\tag{3.3}$$

Two point objects separated less than this distance cannot be resolved. A graphic representation of resolvable and unresolvable points according to the Rayleigh criterion is given in figure 3.1.
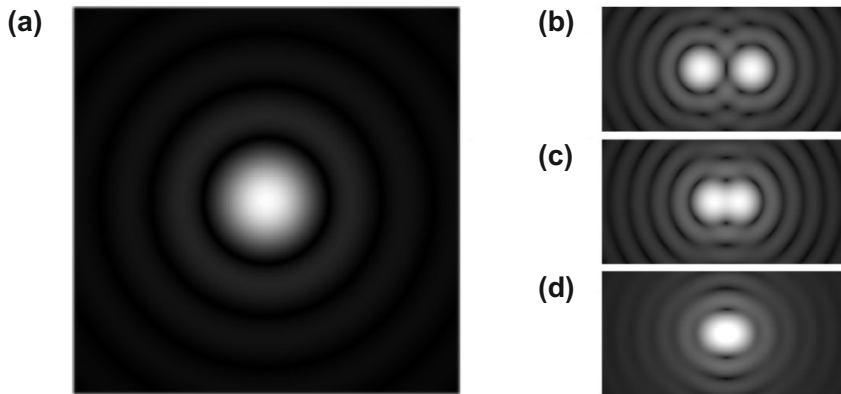
Figure 3.1: Airy pattern and Rayleigh criterion. **(a)** Airy pattern of a single emitter. **(b)** Airy patterns of two emitters that are sufficiently separated to be easily distinguished. **(c)** Airy patterns of two emitters that can just be distinguished according to Rayleigh criterion. The maximum of one Airy disk is located in first minimum of the other Airy disk. **(d)** Airy patterns of two emitters that are not distinguishable any more according to the Rayleigh criterion. Figures adapted under free license from Wikipedia [33, 34].

For both the Abbe and the Rayleigh criterion, resolution increases with decreasing wavelength and increasing numerical aperture. However, the radius of the central disk of the Airy pattern always remains finite and imposes a resolution limit to conventional optical microscopy

of about 200 nm.

Obtaining structural information of an object is only possible if the spatial structure of interest is larger than the resolution limit. For many biological structures this is not the case, as subcellular structures show a range of lengths scales from nanometers to microns. Therefore, those structures cannot be resolved with conventional light microscopy, but require more advanced techniques to be studied in detail.

3.2 Single-Molecule Localization Microscopy

Single-molecule localization microscopy (SMLM) refers to a group of fluorescence microscopy techniques that achieve a resolution higher than the diffraction limit. These super-resolution techniques include stochastic optical reconstruction microscopy (STORM, [32]), direct stochastic optical reconstruction microscopy (dSTORM, [35, 36]), photoactivated localization microscopy (PALM, [31]) and fluorescence photoactivated localization microscopy (fPALM, [37]). The following sections will give a short introduction into the phenomenon of fluorescence, fluorescent labeling and the principle behind single-molecule localization microscopy.

3.2.1 Fluorescence

Fluorescence is a process of absorption and emission of electromagnetic radiation that occurs in certain molecules that are referred to as fluorophores. A full description of this phenomenon can only be given in the framework of quantum mechanics. A simplified model of fluorescence will be described in the following and is illustrated in figure 3.2. A fluorescent molecule can be excited from its electronic ground state S_0 to a higher electronic state by the absorption of an incoming photon of energy $\hbar\nu_{ex}$, where $\hbar$ is the Planck constant and ν_{ex} the excitation frequency. Some of the energy is stored in vibrational states and lost as heat E_{heat} due to dissipative processes. The transition can be described by

$$S_0 + \hbar\nu_{ex} \rightarrow S_1 + E_{\text{heat}}. \tag{3.4}$$

After a short delay time of about one nanosecond, the molecule relaxes back to its ground state. The relaxation energy is released by the emission of a photon of energy $\hbar\nu_{em}$, where ν_{em} is the emission frequency. Again, some energy is lost due to dissipation. The transition can be described by

$$S_1 \rightarrow S_0 + \hbar\nu_{em} + E_{\text{heat}}. \tag{3.5}$$

Due to radiation-free loss of energy, it holds that $\hbar\nu_{ex} > \hbar\nu_{em}$. Therefore, the wavelength of emitted photons is longer than the wavelength of absorbed photons. This shift of wavelengths is commonly referred to as Stokes shift (see figure 3.2).

Many fluorescent molecules can also relax to their ground state via an alternative energy pathway. There is a small possibility of intersystem crossing via which the fluorophore can undergo a radiation-free transition from the excited singlet state to a triplet state of lower

energy. This triplet state can be quite stable due to low transition rates to the ground state. Energy can be stored in this triplet state for several milliseconds up to minutes or hours. Finally, the energy is released as a photon and the molecule returns to its ground state. This phenomenon is referred to as phosphorescence. While the fluorophore resides in the triplet state it cannot be excited and hence, does not release any photons. This results in long dark times before repeated observation.

Commonly used fluorophores show specific absorption and emission spectra that are typically within the visible spectrum. The selected excitation laser has to match the absorption spectrum of the fluorophore used in the experiment. Due to the Stokes shift, the emission spectra is shifted towards higher wavelengths compared to the absorption spectra. This allows for separating reflected excitation from emission light through the use of specific filters. However, the two spectra typically still show some overlap.

An important factor concerning fluorescence is that a fluorophore may lose its ability to absorb and emit photons. Irradiation can trigger irreversible chemical changes in the fluorophore, destroying its fluorescent properties. This process is commonly referred to as photobleaching. The resistance of a fluorophore against photobleaching is described by its photostability.
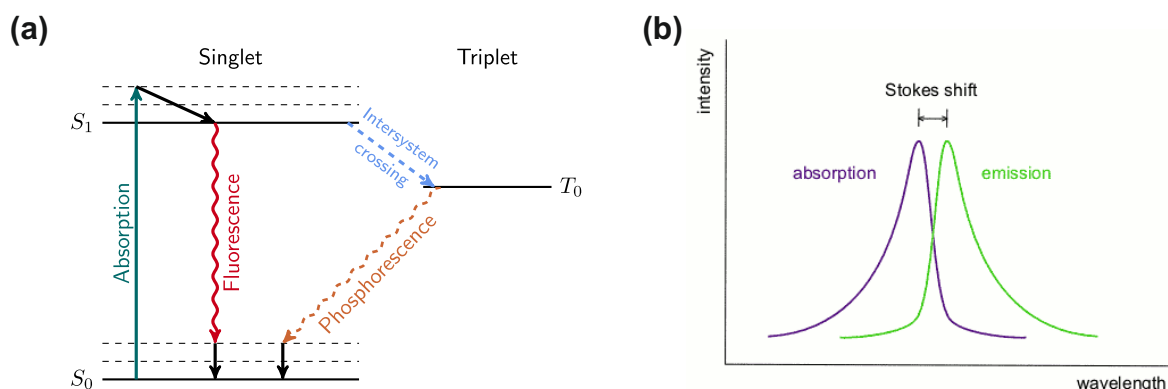
Figure 3.2: Fluorescence. **(a)** Jablonski diagram outlining a simplified model of fluorescence. The fluorophore can be excited from its ground state S_0 into a state of higher energy S_1, and relax back to the ground state by emission of a photon. With a small probability relaxation can also happen via a triplet state T_0, resulting in longer dark times. **(b)** Stokes shift. The emission spectrum of the fluorophore is shifted towards higher wavelengths compared to the absorption spectrum (figure adapted under free license from Wikipedia [38]).

3.2.2 Fluorescent probes and labeling

For performing fluorescence microscopy, the biomolecules of interest have to be labeled with fluorescent molecules in order to be detectable in the experiment. A variety of fluorophores is available, each of them showing specific characteristics like excitation and emission spectra, brightness, photostability and blinking behavior. When performing an experiment, the used fluorophore has to be chosen carefully in order to be suitable for the desired task and technique. An important aspect to be taken into account is that the binding of a fluorophore to a molecule

of interest must not alter the molecule's characteristics or impair a protein's functionality. Otherwise, the results and findings of the performed experiment will be impacted and in the worst case distorted. In the following, a short overview of the most common labeling techniques is given.

Fluorescent proteins. A fluorescent protein can be genetically attached to proteins of interest. For this, the gene of the fluorescent protein is introduced into the cell via transfection and genetically fused to the target protein. In the following, the fusion protein is expressed by the cell. Both membrane and intracellular proteins can be labeled this way. The first fluorescent protein used as a fluorescent marker was the green fluorescent protein (GFP), discovered by Shimomura et al. in the 1960s [39] and isolated from the jellyfish *Aequorea victoria*. Nowadays, a large number of derivates from GFP exist that each show distinct properties suitable for specific tasks.

Organic dyes. Organic dyes are small fluorescent molecules that commonly show high brightness and good photostability. They can be used for specific labeling of biomolecules by either covalent conjugation or immunolabeling. For immunolabeling, a primary antibody binds to the protein of interest. The fluorescent dye is either directly fused to the primary antibody or bound to it via a secondary antibody.

Quantum dots. Quantum dots are semiconductor nanoparticles. Many types of quantum dots also show fluorescence and hence, can be used as markers in fluorescence microscopy. Their optoelectronic properties can be easily tuned by varying their size and shape. However, quantum dots are less suitable for cell biology experiments due to their relatively large size, which makes it difficult to reach molecules of interest.

3.2.3   Single-molecule localization

In single-molecule localization microscopy, the position of single fluorophores has to be determined. To make this possible, adjacent fluorescent molecules need to be far enough apart in order to be resolvable as single emitters. A single point-like emitter is represented by its point spread function (compare section 3.1). The photon intensity has the shape of an Airy pattern given by equation (3.1). The Airy disk, the central spot of the pattern, contains approximately 85 percent of the signal. The other rings of the pattern are usually hardly observable and dominated by background noise. Therefore, the detected intensity of a single fluorescent probe is usually approximated by a 2D Gaussian function that shows a good fit for the overall decreasing intensity of the Airy disk in radial direction [5]. From this fit, the maximum of the intensity can be determined with subpixel precision. The obtained coordinates are taken as the molecule's position.

The Gaussian fit and hence also the localization precision depend on various factors of signal quality. Different formulas for the estimation of the localization precision Δx have been
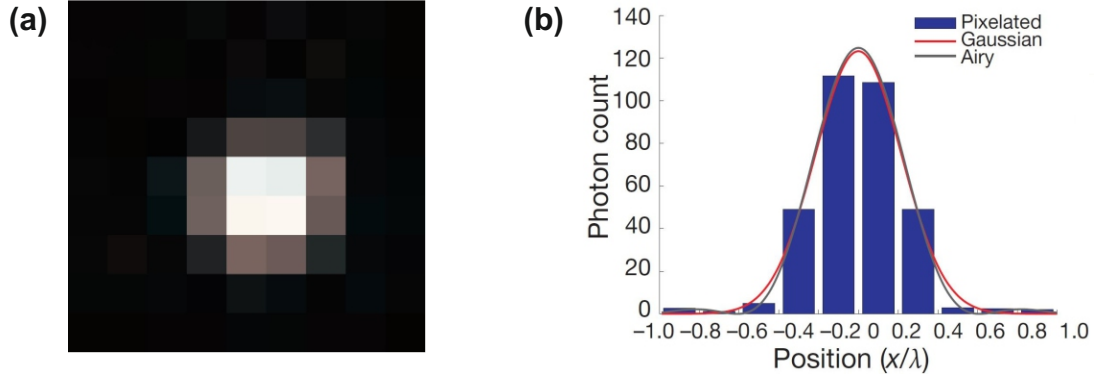
Figure 3.3: Fitting of the point spread function. **(a)** Pixelated image of a fluorophore. **(b)** Approximation of a cross-section of the pixel intensities from **a** with a Gaussian function and a Airy function, respectively. Figures adapted from Small and Stahlheber [40].

proposed in the literature. A simple estimation is given by

$$\langle (\Delta x)^2 \rangle = \frac{s^2}{N},$$

(3.6)

where s is the standard deviation of the fitted Gaussian distribution and N is the number of detected photons. A more elaborate formula suggested by Thompson et al. [5] does not only take into account the number of collected photons N, but also pixel size a and background noise b^2 and calculates the error in localization as

$$\langle (\Delta x)^2 \rangle = \frac{s^2}{N} + \frac{a^2/12}{N} + \frac{8\pi s^4 b^2}{a^2 N^2} \ .$$

(3.7)

According to this formula, a higher number of detected photons and smaller pixel size will in theory further increase the localization precision. In practice however, their will always remain a small error in localization due to finite acquisition time and pixel size. In addition, factors like diffusion of fluorophores and stage drift during acquisition time further reduce the localization precision.

Another approach that provides more accurate estimations of the localization precision was presented by Smith et al. [41]. The method iteratively computes position and intensity of single fluorophores and converges to the maximum likelihood estimate. Uncertainties of the parameters are determined by calculating their Cramér-Rao lower bound (CRLB) [42].
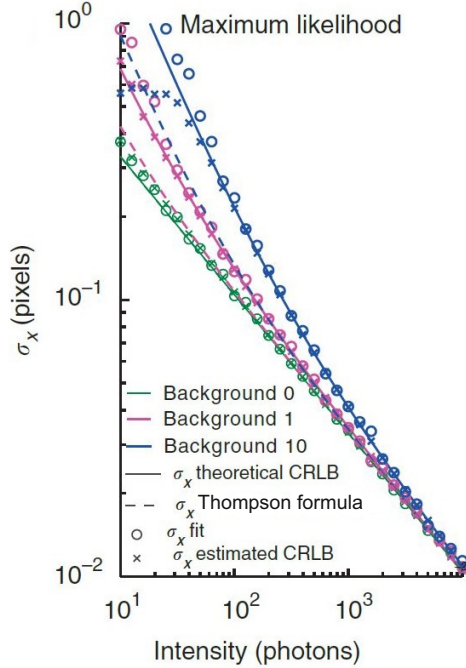
Figure 3.4: Estimation of localization precision. Comparison of the Thompson formula [5] and the approach of determining uncertainties by calculating the Carmér-Rao lower bound (CRLB) presented by Smith et al. [41]. If background fluorescence is taken into account, the Thompson formula leads to overly optimistic estimates of localization precision. Figure adapted from Smith et al. [41].

3.2.4 Principle of dSTORM

Single-molecule localization microscopy techniques rely on the stochastic activation of a small subset of fluorescent probes in order to achieve a sub-diffraction-limit resolution of less than 50 nm. There exist several different techniques like STORM [32], dSTORM [35], PALM [31] and fPALM [37], however, they are all based on the same principle, with differences only in the fluorescent probes and microscopes used. The experiments described in this thesis were performed with dSTORM microscopy. Therefore, the principle of single-molecule localization microscopy is explained in the following based on dSTORM.

Before imaging, the sample of interest is densely labeled with conventional fluorescent probes, for example Alexa Fluor organic dyes. Those probes can be switched between a dark (non-fluorescent) and bright (fluorescent) state as shown in figure 3.5. In the bright state, the fluorophore can cycle between the singlet ground state and excited state showing fluorescence by the emission of photons. Upon irradiation with a light of appropriate wavelength the fluorophore is transferred to its triplet state that is non-fluorescent.

The application of single-molecule localization techniques is usually restricted to fixed cells, unless probe movement during image acquisition is small compared to the desired resolution. For dSTORM experiments on fixed cells the sample is embedded in a buffer containing millimolar concentrations of thiol (e.g. β-mercaptoethylamine, MEA). The thiolate anion (RS⁻) acts as an electron donor and can reduce the triplet state of the fluorophore, forming a radical anion. The

reduction of the triplet state is facilitated upon irradiation.

The radical anion can be oxidized by molecular oxygen, which transfers the fluorophore back to its singlet ground state and recovers its fluorescence. However, the radical anion is relatively stable, in particular on removal of oxygen, and the fluorophore can be trapped in its dark state for several seconds to hours. In order to stabilize the dark state, the buffer, in which the sample is embedded, is depleted in oxygen. The recovery of the bright state is facilitated upon irradiation at a wavelength of 405 nm.

The dSTORM imaging process is shown schematically in figure 3.6. Initially, a laser pulse is applied to transfer all fluorophores from the bright state to their dark, non-fluorescent state. Then, a stochastic small subset of all fluorophores is transferred back to the bright state. This can happen either spontaneously or photoinduced upon irradiation with an activation laser pulse of appropriate wavelength, typically 405 nm. For sufficiently low probabilities of fluorophore activation, the fluorophores that are in their bright state will statistically be spaced further apart than the diffraction limit, thus allowing precise localization.

Fluorescence is excited by an excitation laser pulse matching the excitation spectrum of the used fluorophore. Each frame yields a matrix of photon counts corresponding to the intensity distributions at the CCD chip. From this information, the locations of excited fluorophores can be determined. The position of the molecule is calculated by fitting a Gaussian function to the point spread function of the emitter and finding its maximum. All fluorophores in the bright state are subsequently transferred back to their dark state. The process of activation, excitation and subsequent return of the fluorophores to their non-fluorescent state is repeated several thousand times. In each iteration, coordinates of molecule positions are obtained by the
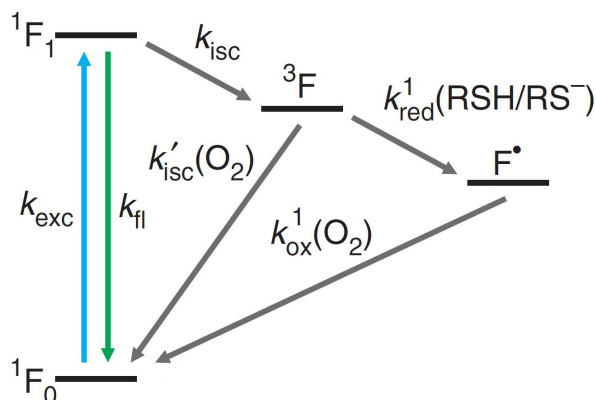
Figure 3.5: Reversible photoswitching of Alexa Flour organic dyes. In its bright state, the fluorophore can cycle between the singlet ground state F_0 and an excited state F_1 and emit photons. Upon irradiation the fluorophore can be transferred to a dark triplet ^3F state with the rate k_{isc}. From this triplet state, the fluorophore can either relax back to its singlet ground state with a rate k'_{isc} through a reaction with oxygen, or be transferred to its radical anion state $F^\bullet$ with a rate k_{red} through a reaction with a thiolate. The radical anion is not very reactive and hence, stable for several seconds. With a rate k_{ox} the anion is oxidized by oxygen and recovers to its singlet ground state. In the singlet state, the fluorophore shows fluorescence again. Figure adapted from van de Linde et al. [35].

localization of a subset of fluorophores. The acquisition rate of the frames is usually around 10–500 Hz. Finally, all acquired localizations from typically thousands of image frames are combined and used to reconstruct the final image of the structure under investigation. [35]

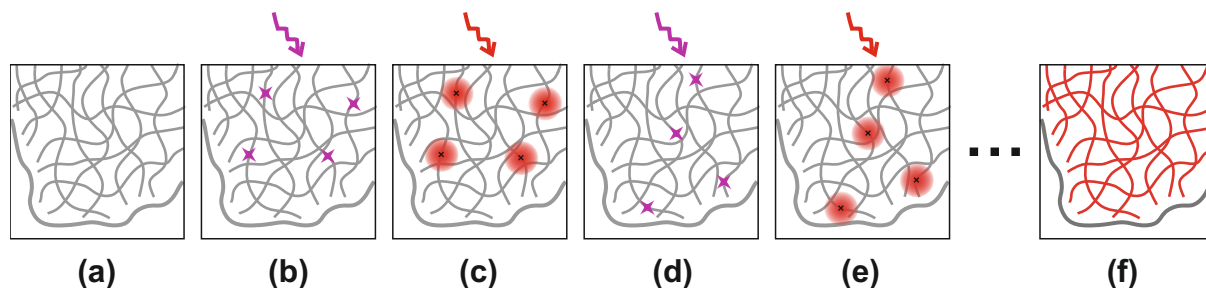Figure 3.6: Principle of dSTORM. **(a)** The structure of interest is densely labeled with photo-switchable fluorophores. First, all fluorophores have to be transferred to their non-fluorescent dark state by a laser pulse of appropriate wavelength. **(b)** Activation of a subset of fluorophores occurs either spontaneously or is photoinduced by an activation laser pulse of wavelength around 400 nm. **(c)** Excitation of fluorophores with an excitation laser pulse. Fluorophores emit fluorescence and are subsequently transferred back to their dark state. The positions of molecules is determined by fitting Gaussian functions to the detected intensity distributions and finding their maximum. **(d, e)** The process of activation, localization and deactivation is iterated for typically several thousand times. **(f)** All acquired localizations are combined and result in a high resolution image reconstruction. Figure created based on figure 4.1 in Hinterdorfer and Van Oijen [43].

In ideal experimental conditions, spatial resolution of single-molecule localization microscopy is only limited by the accuracy of each localization. The localization precision depends on factors like the number of detected photons, pixel size and background noise, as discussed in more detail in section 3.2.3.

For two-color single-molecule microscopy, the sample of interest is labeled with two different kinds of fluorophores that show distinct excitation and emission maxima, for example the organic dyes Alexa Fluor 488 and Alexa Fluor 647. Both kinds of fluorophores can be switched into their bright state by an activation laser of 405 nm. Then, the fluorophores of different colors are imaged alternating between excitation lasers with wavelengths of 488 nm and 640 nm, respectively. The emitted light can be distinguished according to its wavelength and is separated into different channels by the use specific filters. [43]

3.3 Total Internal Reflection Fluorescence (TIRF) Microscopy

An important aspect for achieving optimal resolution in a fluorescence microscopy experiment is a high signal-to-noise ratio. Background signal is caused by thermal background noise on the camera chip, but can also be due to autofluorescent endogenous metabolites contained in the cell that are difficult to distinguish from fluorescently tagged molecules of interest. Total internal reflection fluorescence (TIRF) microscopy offers a way to reduce this background fluorescence from inside the cell by modifying the excitation pathway [44, 45]. The technique allows for exciting only those fluorescent molecules that reside in the region near the glass slide. Hence, it is an optimal tool for studying the plasma membrane of attached cells. The method of TIRF can be combined with many fluorescence microscopy techniques, among others with super-resolution techniques like STORM and PALM.

The principle behind TIRF is based on Snell's law of refraction that describes the relationship of the angle of incidence θ_1 and refraction θ_2 for an electromagnetic wave that passes the boundary between two isotropic media of different refractive indices n_1 and n_2, respectively, as

$$n_1 \sin(\theta_1) = n_2 \sin(\theta_2). \tag{3.8}$$

With increasing angle of incidence θ_1, also the angle of refraction θ_2 increases. The angle of incidence for which the angle of refraction equals $\theta_2 = 90°$ is called the critical angle θ_{crit}. In this case, Snell's law simplifies to

$$n_1 \sin(\theta_{crit}) = n_2 \sin(90°) = n_2. \tag{3.9}$$

If $n_1 > n_2$ we can solve this equation for θ_{crit} and obtain

$$\theta_{crit} = \arcsin\left(\frac{n_2}{n_1}\right). \tag{3.10}$$

Hence, a critical angle exists if $n_1 > n_2$, which means that light passes from a medium of higher density into a medium of lower optical density. For all angles of incidence greater than the critical angle the incident light beam is totally reflected. However, at the interface of the two media, some of the incident energy passes into the other medium and penetrates it up to a depth of 100–200 nm for light in the visible spectrum. The resulting electromagnetic field is called evanescent field or evanescent wave and is visualized in figure 3.7. Its intensity I shows a distribution that is perpendicular to the interface of the two media and decays exponentially according to

$$I(z) = I_0 \, e^{-z/d}, \tag{3.11}$$

where z is the distance from the interface and d is the characteristic penetration depth. The characteristic penetration depth d depends on the wavelength of light λ, the angle of incidence

θ of incoming photons and the refractive indices n_1 and n_2 of the media, and is given by

$$d = \frac{\lambda}{4\pi} \left(n_1^2 \sin^2(\theta) - n_2^2\right)^{-1/2} .$$
(3.12)

With increasing angle of incidence θ the penetration depth decreases, which leads to further reduction of background fluorescence when imaging a cell membrane.

In the case of TIRF microscopy, the excitation light is reflected at the interface between the microscope slide (with an refractive index of $n_1 \approx 1.5$) and the aqueous specimen (with an refractive index of $n_2 \approx 1.33$). Hence, total reflection occurs at a critical angle of approximately $\theta_{crit} \approx 60°$. The resulting evanescent field excites fluorophores near the interface, while avoiding the excitation of autofluorescent molecules or other fluorophores further away from the surface. This leads to a significant reduction of cytosolic background signal and hence a higher signal-to-noise ratio, which improves localization precision of single-molecule localization. Therefore, TIRF microscopy is ideally suited for studying molecules in the cell plasma membrane.

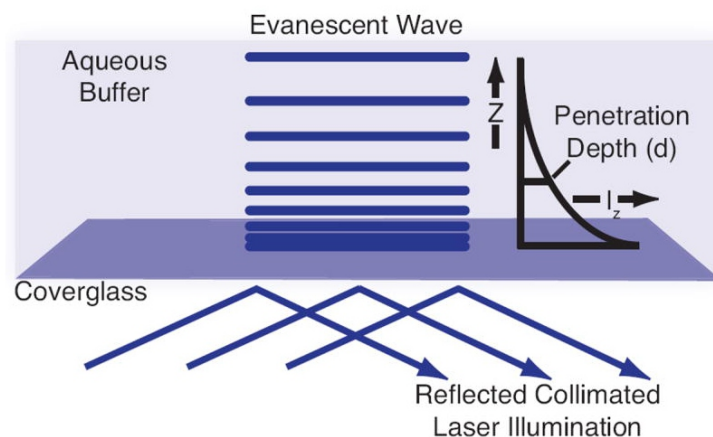Figure 3.7: Principle of TIRF microscopy. The sample is illuminated with a laser at an angle steep enough to achieve total reflection. Some of the incident energy passes the interface of the two media as evanescent wave and penetrates the sample up to a depth of typically 100–200 nm, allowing to excite fluorophores near the glass slide while avoiding background fluorescence. Figure adapted from Fish [46].

Chapter 4

Materials and Methods

4.1   Simulations

4.1.1   Simulation of single-molecule localization experiments

For testing methods distinguishing between randomly distributed and clustered molecules on the cell membrane, we developed MATLAB programs that simulate a region of interest on the cell membrane with a given distribution of molecules. In the following, only those features of the programs are described that were used in simulations performed for this thesis.

Proteins on the cell membrane are labeled via antibodies that carry one of two kinds of fluorescent probes. Molecules bound to the first and second type of fluorescent probe are referred to as carrying the label A and B, respectively. In an experiment, the fluorescent probes can be separated into two different color channels due to their distinct emission spectra. In the simulation, the two color channels are simulated separately taking into account all labels of the corresponding type. In a first approach, we assume experimental conditions in which the cell is fixed and neglect any residual diffusion of the molecules [24]. Stage drift and chromatic aberration can be simulated optionally.

All simulations were developed and carried out in MATLAB version R2016b (TheMath-Works, Inc., Natick, United States). Random numbers were generated with a pseudorandom number generator provided by MATLAB that was initiated with the command `rng('shuffle', 'twister')`. Those input parameters choose the Mersenne Twister as random number generator (option `'twister'`) and seed it based on the current time (option `'shuffle'`).

Simulation region

The code allows for the simulation of a part of the cell membrane on a quadratic region of interest (ROI). The size of this region can be chosen as an input parameter. A margin of twice the size of the upper limit of the localization precision is added to avoid biases at the edges of the region of interest. Periodic boundary conditions are applied in order to conserve mass and not to lose any molecules, for example due to stage drift.

Distribution of molecules

The number of molecules in the region of interest can be assigned as an input parameter. This given number of molecules is then spread over the simulated region according to a defined distribution. The distribution of the molecules is also set as an input parameter and can be one of the options 'random', 'oligomer' or 'cluster'.

In the case 'random', x- and y-coordinates of the molecule positions are assigned using pseudorandom numbers that spread all molecules randomly over the simulation region. In the case 'oligomer', there are additional input parameters that define the number of monomer units that constitute a molecular complex, and the fraction of monomers on the cell membrane. For dimers, trimers, and tetramers, the number of monomer units in one molecular complex are $2, 3$, and 4, respectively. First, the oligomers are spread randomly over the region of interest. All monomers that belong to the same oligomer are assigned to the same molecule position. Then, the remaining number of monomers is spread randomly. The option 'cluster' simulates clustering on the plasma membrane. The number of clusters, cluster radius and fraction of molecules residing inside clusters can be specified as input parameters.

Fluorescent labeling

The code is designed to simulate immunofluorescence staining of cells [47]. For this method, antibodies that target specific cellular proteins are exposed to the cell. These antibodies are covalently bound to fluorescent dyes that can be detected and thus reveal information about the localization of the protein of interest in the cell.

However, not necessarily every simulated protein is assigned to a fluorescent label. In experiments, it can happen that either a molecule has no antibody bound to it, or the antibody binding to the molecule carries no or no functioning fluorescent dye. The simulation takes this into account as a combined effect. Each antibody is assumed to be bound to a fluorescent probe and is simulated together with it. Every molecule of interest is either unlabeled (no antibody binds to it), or labeled (exactly one antibody binds to it). In the simulations performed for this thesis, we do not allow for multiple antibodies to be bound to the same molecule and hence, a molecule cannot carry fluorescent dyes of both types. The labeling efficiency η defines how many of the simulated molecules carry an antibody with a fluorescent dye bound to it and can be set as an input parameter.

The code allows for the simulation of a two-color single-molecule localization experiment, hence, there are two different kinds of fluorescent labels. For reasons of simplicity, these labels are termed label A and label B in the following. Let α denote the fraction of all labels that are of type A, and β the fraction of labels of type B. Then, the numbers M_A and M_B of molecules that carry fluorescent dyes of type A and B, respectively, are given by

$$M_A = \alpha \, \eta \, M$$

and

$$M_B = \beta \, \eta \, M,$$

where M is the total number of simulated molecules. Those molecules that are bound to an antibody and hence, carry a label, are determined by chance.

The code also considers unspecifically bound antibodies that do not bind to the targeted protein but some cellular structure or the glass slide. The number of those unspecifically bound labels can be set as an input parameter. The fact that an antibody can be labeled with multiple fluorescent dyes of the same color is not simulated explicitly, but is accounted for in the blinking statistics used for the simulation of overcounting of molecules.

Overcounting

In a single-molecule localization experiment fluorophore blinking leads to the overcounting of molecules, as the same molecule is detected multiple times.

Molecules that carry a fluorescent label of type A are detected in color channel 1, those that carry label B are detected in color channel 2. The simulation treats localizations in both color channels separately. All localizations for one molecule are simulated in several steps. First, the number of blinks for each labeled molecule is determined by generating random numbers according to a given blinking distribution specified in the input parameters. In addition to the number of blinks, also the frame number of the first localization and on- and off-times are needed for simulating overcounting. The on- and off-times are the number of consecutive frames in which a fluorophore is in the bright state or dark state, respectively. Random numbers for all those variables are generated based on the given input distributions of a specific fluorophore. All required input distributions can be given either as histograms or probability density functions, and already include the possibility of multiple fluorophores per antibody.

The blinking distributions used in this thesis were determined experimentally in our laboratory for the following commercial fluorescent probes.

PS-CFP2. The fluorescent protein PS-CFP2 is photoswitchable between a cyan and a green fluorescent state. The excitation and emission maxima of both states of the protein are given in table 4.1.

	PS-CFP2	
	before photoactivation	after photoactivation
Fluorescence color	cyan	green
Excitation max. [nm]	400	490
Emission max. [nm]	468	511

Table 4.1: Excitation and emission maxima of PS-CFP2. Data retrieved from Evrogen [48].

Alexa Fluor 647. The organic dye Alexa Fluor 647 exhibits excitation and emission spectra at wavelengths around 640 nm (red). Excitation and emission maxima are given in table 4.2. Alexa Fluor 647 can be used as a label in combination with various antibodies, for example TCR β chain antibody (clone H57-597) or CD3 monoclonal antibody (clone KT3), in the following

referred to as Alexa647-H57 and Alexa647-KT3, respectively. As the number of fluorescent dyes per antibody varies dependent on the kind of antibody that is used, also the overall blinking behavior is different.

	Alexa Fluor 647
Fluorescence color	red
Excitation max. [nm]	650
Emission max. [nm]	665

Table 4.2: Excitation and emission maxima of Alexa Fluor 647. Data retrieved from Thermo Fisher Scientific [49].

Blinking statistics including the number of blinks, the frame number of the first localization and the on- and off-times for the above described fluorescent probes are given in the appendix A.2. From these distributions, random numbers for the blinking behavior of a fluorophore can be generated. For each molecule, the number of its detections is acquired and each localization can be allocated to a certain frame. The total simulated number of frames can be set as an input parameter, but should be chosen in accordance with the used blinking statistic.

Localization precision

The position of a detected fluorophore cannot be determined exactly, but only with a limited positional accuracy (see section 3.2.3). The simulation code takes this into account and displaces each localization by a localization error.

For obtaining the coordinates of a localization, the coordinates of the molecule's actual position is displaced in x- and y-direction by random displacements Δx and Δy that are realizations of a random variable $X_{\Delta x}$ that is distributed according to a normal distribution with mean value 0 and standard deviation δ, the positional accuracy for the considered localization:

$$X_{\Delta x} \sim \mathcal{N}(0, \delta).$$

The coordinates of the single-molecule localization are hence given by

$$(\tilde{x}, \tilde{y}) = (x + \Delta x, y + \Delta y).$$

The positional accuracy depends on various factors, for example pixel size, background noise and photon count. The photon count may vary for each fluorophore and hence, the positional accuracy δ is different for each localization. Therefore, we simulate δ to follow a random variable $X_{p.a.}$ that is distributed according to a normal distribution

$$X_{p.a.} \sim \mathcal{N}(\mu_{p.a.}, \sigma_{p.a.}), \qquad (4.1)$$

with mean value $\mu_{p.a.}$ and standard deviation $\sigma_{p.a}$ that can be set as input parameters for the simulation. As localizations with a very low positional accuracy do not provide trustworthy

results, these localizations are usually omitted in data analysis of experiments. We simulate this by truncating the above given normal distribution (4.1) to values between a lower limit l_{low} and an upper limit l_{up} that can be chosen as input parameters. For each single-molecule localization a value δ for the localization precision is drawn randomly according to the specified distribution.

After calculating the positions of all localizations, periodic boundary conditions are applied in order to assure that all localizations lie within the simulated region and to avoid any biases due to omitted localizations at the edges arising from molecules outside of the simulated region.

Stage drift

In the experimental setup it may occur that the microscope stage is subject to drift and, hence, the position of the sample is displaced relative to the objective. This drift may be caused by variations of room temperature or mechanical instabilities of the optical setup [43]. Stage drift is accounted for in the code by displacing all localizations by a vector describing the direction of drift. The vector of drift in x- and y-direction for each frame is determined randomly following a truncated normal distribution. Mean, standard deviation, as well as lower and upper bounds for this probability distribution can be set as input parameters. If all values are set to be greater to zero, drift occurs in a specific direction. The resulting coordinates of localizations in a certain frame number n are calculated by cumulatively adding the displacements due to stage drift over all precedent frames to the original position of localizations:

$$(\tilde{x}, \tilde{y}) = (x, y) + \sum_{i=1}^{n} (\Delta x_i, \Delta y_i),$$

where Δx_i and Δy_i are the displacements due to shift during acquisition of frame number i. Again, periodic boundary conditions are applied so that no molecules and their localizations drift out of the simulated region.

Diffuse background

In a single-molecule localization experiment localizations do not only arise from fluorescent labeled molecules or unspecifically bound labels, but can also be due to (intracellular) background fluorescence emission or detector noise. Those background localizations are accounted for in the simulation code by generating single localizations that are distributed randomly over the whole region of interest. The number of those background localizations can be set as input parameter.

Chromatic aberration

In multicolor imaging chromatic aberration occurs due to different refractive indices of optical lenses for different wavelengths of light. There exist two different types of chromatic aberration, longitudinal (axial) chromatic aberration and lateral (transverse) chromatic aberration. Due to longitudinal chromatic aberrations light of different wavelengths is focused at different

focal lengths. This leads to blurring of the image. Lateral chromatic aberration causes light of different wavelengths to be focused at different positions in the focal plane. The code allows for simulation of lateral chromatic aberration, as only this form of aberration leads to relative distortions of the images of different color channels. A graph illustrating the principle of lateral chromatic aberration is shown in figure 4.1. Lateral chromatic aberration leads to radial distortion of the image. Magnification is zero in the center and increases radially. The increase of magnification for each plane of a certain color depends on its wavelength. In part, lateral chromatic aberration can be corrected for by the use of fiducial markers and appropriate post-processing of obtained experimental data. However, these corrections never lead to perfect alignment of both color channels and residual errors remain.

Lateral chromatic aberration is simulated by displacing all localizations in color channel 2 according to their position by the vector field

$$f(x, y) = (c_x, c_y) := ((x - x_0) \cdot c, (y - y_0) \cdot c), \tag{4.2}$$

where c is the aberration for a certain light wavelength in nm per nm off the optical axis and (x_0, y_0) are the coordinates of the optical axis where chromatic aberration is zero. The parameter c and the point of the optical axis can be specified as input parameters. Figure 4.1 shows the displacement vectors depending on the position in the ROI due to chromatic aberration.
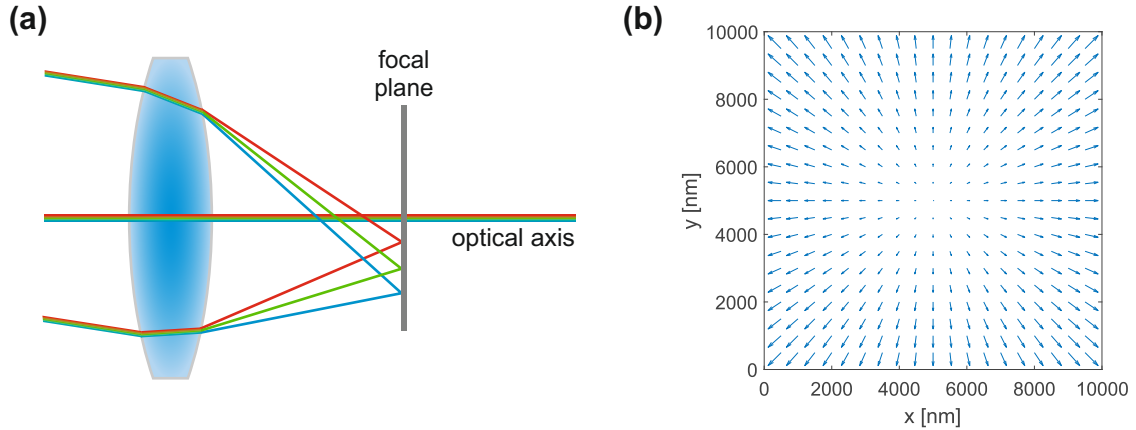
Figure 4.1: Lateral chromatic aberration. **(a)** Light of different wavelengths is focused on different points on the focal plane. **(b)** Vector field of displacement vectors. The displacements increase with the distance from the optical axis.

Region of interest

Finally, for obtaining just those localizations of the simulation that lie within the specified region of interest, all localizations that lie outside this region are neglected.

4.1.2   Input parameters of simulation

This section gives an overview of the most important input parameters to run a simulation of a single-molecule localization microscopy experiment.

Region of interest

The parameter a is the side length of the quadratic region of interest and is given in nm.

Number of molecules

The parameter N_{mols} specifies the number of molecules on the cell membrane per μm^2.

Distribution of molecules

Different types of distributions of the molecules of interest on the cell membrane are implemented. The option 'random' simulates randomly distributed molecules, whereas the option 'oligomer' simulates molecules that are present as oligomers. In the case 'oligomer', additionally, the degree of oligomerization ($n_{\mathrm{oligo}} = 2$ for dimers, $n_{\mathrm{oligo}} = 3$ for trimers etc.) and a possible fraction ζ of monomeric molecules (value between 0 and 1) can be specified. The option 'cluster' simulates clustering, with variable numbers of clusters, cluster radius (given in nm), and fraction of molecules (between 0 and 1) residing inside the clusters.

Labeling efficiency

The labeling efficiency η (with values between 0 and 1) specifies the percentage of simulated molecules that are actually bound to a functional fluorescent dye. In practice, labeling efficiency does not reach 100 percent.

Label ratio

The molecules can be labeled with fluorophores of two different kinds. The ratio of fluorescent labels of type A and type B can be set via the input parameter α with a value between 0 and 1, specifying the fraction of labels of type A. The fraction β of labels of type B follows from the equation

$$\alpha + \beta = 1. \tag{4.3}$$

Blinking statistic

The blinking statistic is given as a MATLAB structure with the fields `type`, `num`, `start`, `ton` and `toff`. The type specifies if the blinking statistics are given as probability density functions ('pdf') or histograms ('hist'). The field `num` determines the number of blinks per label, `start` the frame of the first detection of a particular fluorophores, and `ton` and `toff` the on- and off-times, that is the number of frames a fluorophore is in its bright or dark state, respectively.

Localization precision

The positional accuracy is simulated following a truncated normal distribution. The mean $\mu_{p.a.}$, standard deviation $\sigma_{p.a.}$ and lower and upper bounds l_{low} and l_{up} of this distribution can be set as input parameters.

Stage drift

Stage drift can be included in the simulation by setting the variable `stage_drift=true`. The vector of drift in x- and y-direction per frame is given in nm and drawn from a truncated normal distribution. Mean, standard deviation, as well as lower and upper bounds for this probability distribution can be specified as input parameters. If the mean is set to be different from zero, drift occurs in a specific direction.

Number of unspecifically bound labels

The number of unspecifically bound labels per μm^2 can be set for each type of label separately via the parameters $N_{\mathrm{ub,A}}$ and $N_{\mathrm{ub,B}}$.

Number of diffuse background localizations

The parameter N_{bg} specifies the number of background localizations per μm^2 that are distributed randomly over the whole region of interest.

Chromatic aberration

Radial distortions of one color channel due to chromatic aberration can be included in the simulations by setting the variable `chromatic_aberration=true`. The amount of chromatic aberration can be specified as the deviation from the actual position in nm per μm off the optical axis. The point of the optical axis can also be set as an input parameter.

Number of frames

The parameter N_{frames} specifies the number of frames that are recorded in the experiment.

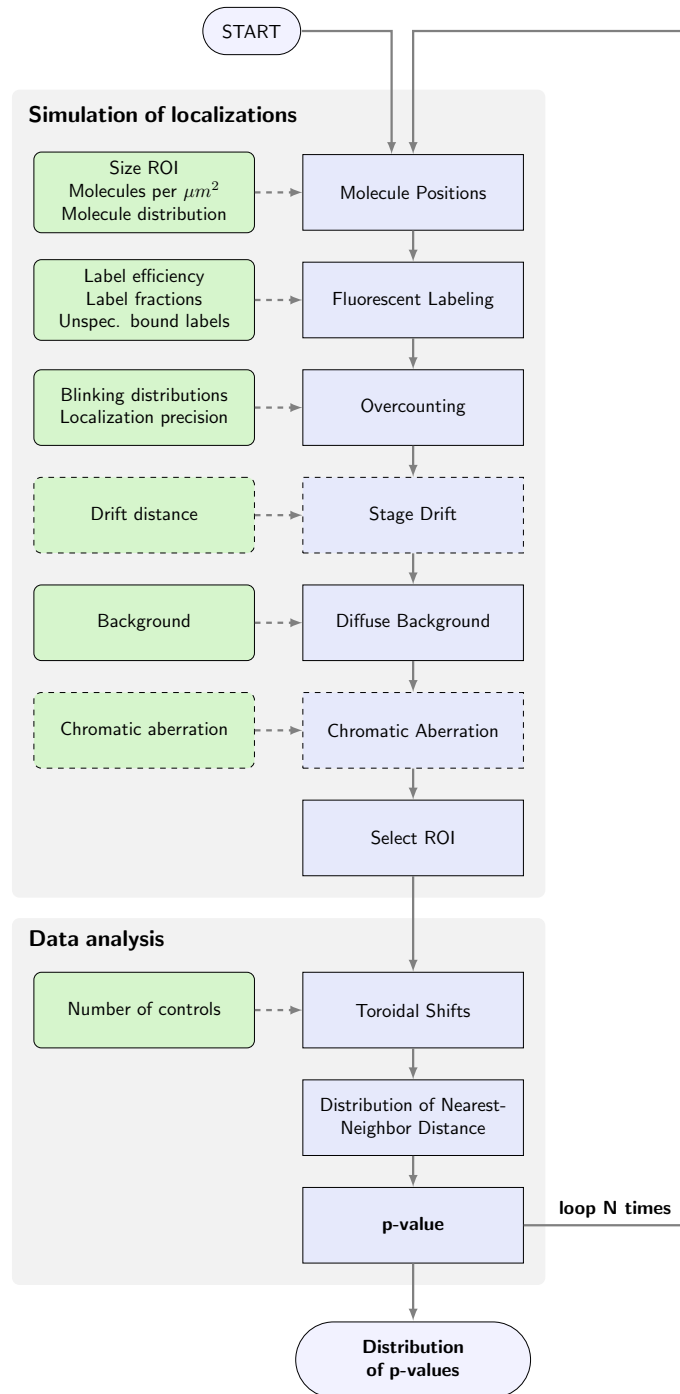Figure 4.2: Flowchart for the simulation of a SMLM experiment and subsequent data analysis. Required input parameters are listed left to the simulation steps (shaded in green). For each set of parameters, $N = 1000$ runs were performed. The p-value obtained for each run is stored and after completion of all runs, the distribution of p-values can be plotted as histogram or cumulative distribution function.

4.2 Experiments

Experiments were performed on HeLa cells transiently transfected with SNAP-tag proteins. The proteins are present either in monomers, dimers, trimers or tetramers. Work on cell culture and single-molecule localization microscopy was carried out by Andreas Arnold and Florian Baumgart.

4.2.1 Microscopy setup

All experiments presented in this thesis were performed on a Zeiss Axiovert 200 inverted microscope (SDT2). A schematic outline of the setup is shown in figure 4.3. We used a near UV-light ion laser (CrystaLaser) with a wavelength of 405 nm for activation of the fluorophores. The laser was modulated via a manual shutter and an acousto optical modulator (AOM). A 640 nm (red) diode laser (Coherent OBIS LX FP 75mW) and a 488 nm (blue) diode laser (Toptica iBeam smart 200mW) were used for excitation of the fluorophores Alexa Fluor 647 and Alexa Fluor 488, respectively. Laser beams of the 640 nm and 488 nm lasers were combined with an OBIS Galaxy Laser Beam Combiner. A dichroic mirror was used to overlay the 405 nm laser line with the combined laser beam of excitation lasers after decoupling from the optical fiber.

A telescope was used to focus the collective laser beam into the back focal plane of the objective (α Plan-Apochromat 100x/1.46 Oil DIC (UV) VIS-IR, tube lens 1.6x). Via a periscope the lasers were coupled into the microscope. The bottom mirror of the periscope was movable, which allowed for parallel shifting of the excitation beam and thus, achieving the required angle of illumination for TIRF microscopy.
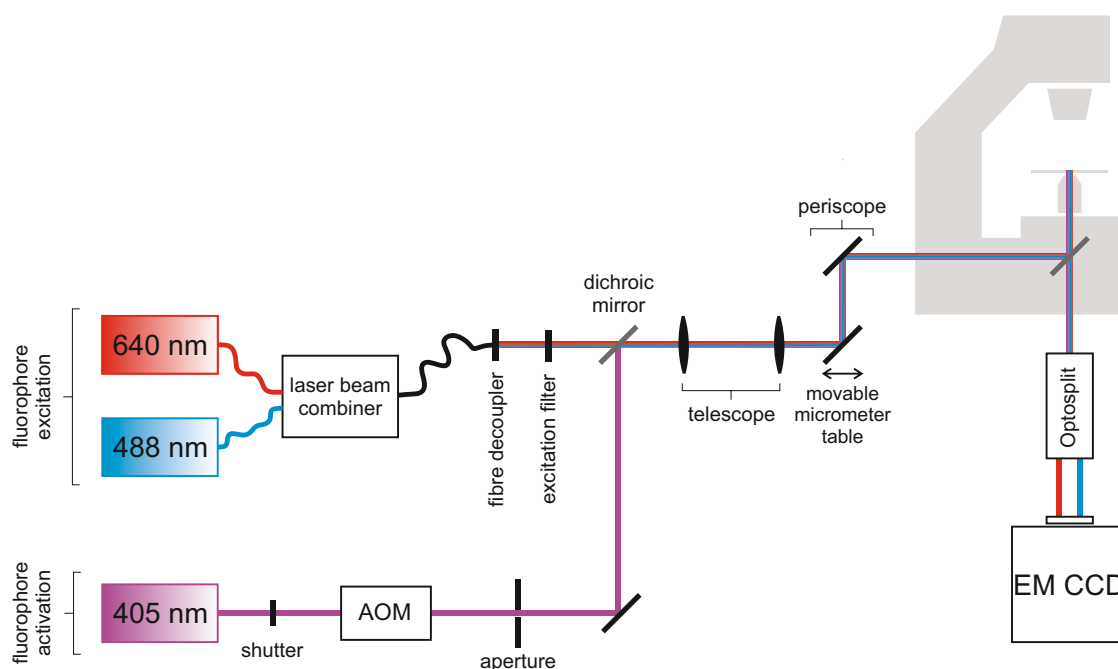

Figure 4.3: Schematic outline of the microscopy setup used for performing the experiments.

Excitation and emission light both passed through the same objective at the bottom of the sample. For the separation of excitation light from the Stokes shifted emission light, a special dichroic mirror was used that reflected the wavelengths of the excitation beam, but transmitted the wavelengths of the emitted light. Moreover, an emission filter blocked remaining stray excitation light. The emitted light was split into separate color channels by a set of filters and dichroic mirrors (Cairn Research Optosplit). Each emission color was projected onto a different region of the camera chip, which allowed for simultaneous multicolor imaging.

4.2.2 Cell culture and transfection

Experiments were performed on HeLa cells (Human cervix adenocarcinoma cells), cultured in Dulbecco's Modified Eagle Medium (DMEM), supplemented with 10% fetal bovine serum (FBS), 2 mM L-glutamine and 1 kU/ml penicillin-streptomycin. Cells were grown under a humidified atmosphere at 37 °C and 5 % CO_2.

For experiments, cells were seeded in Lab-Tek chambers one day prior to the measurements and transiently transfected using TurboFect according to the supplier's instructions for reverse transfection [50]. We tested GPI-SNAP constructs consisting of different numbers of SNAP-tags cloned as tandem repeats. Specifically, we used constructs containing one (1xSNAP-GPI), two (2xSNAP-GPI), three (3xSNAP-GPI) or four (4xSNAP-GPI) SNAP-tags.

4.2.3 Labeling

On the day of the experiment cells were rinsed with Hank's Balanced Salt Solution (HBSS) and colabeled with 50 nM SNAP-AF488 and 1 μM SNAP-AF647, diluted in supplemented DMEM for 30min at 37 °C.

Cells were then extensively washed with HBSS and fixed with 4 % paraformaldehyde (PFA) / 0.1 % glutaraldehyde (GA) for 10 min at room temperature.
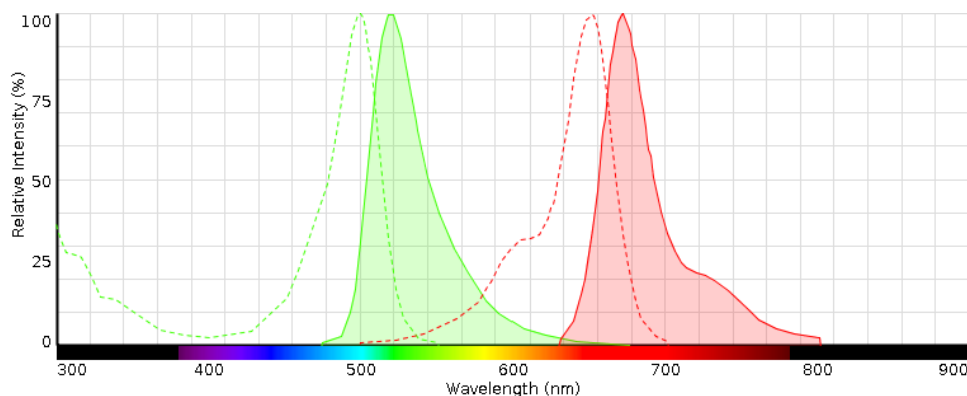

Figure 4.4: Excitation and emission spectra of Alexa Fluor 488 and Alexa Fluor 647. Figure created via the Fluorescence SpectraViewer of Thermo Fisher Scientific [51].

4.2.4 dSTORM imaging

Super-resolution experiments were performed in the presence of OxEA dSTORM buffer (50 mM mercaptoethylamine (MEA), 3 % (v/v) OxyFluor, 20 % (v/v) sodium DL-lactate solution, 1xPBS (phosphate buffered saline), pH 8.0-8.5) [52].

For each imaging stack we recorded 10000 frames per color channel with an illumination time of 1 ms and a delay of 6 ms, alternating between both color channels. The 640 nm and 488 nm laser lines were used for stroboscopic illumination at 1.5–$3 \, \text{kW/cm}^2$. The 405 nm laser at continuous illumination at 20–$30 \, \text{W/cm}^2$ to adjust the number of active fluorophores.

4.2.5 dSTORM analysis

Recorded imaging stacks were analyzed starting with the frame where, judged by eye, illumination had switched most fluorophores to a non-fluorescent dark state and well-separated single molecules could be detected. The same start frame was used for both color channels. To determine the positions of single molecules we used the ImageJ plug-in ThunderSTORM [53], which yielded maps of coordinates of the positions of localizations from both color channels. All parameters used in the ThunderSTORM analysis and for post-processing filters are listed in detail in the appendix A.3.

4.3   Data Analysis

A two-color single-molecule localization experiment results in an image consisting of points of two different colors describing the localizations of color channel 1 and 2, respectively. Experiments using two-color dSTORM were simulated and performed as described in sections 4.1 and 4.2. The acquired image of the cell membrane is the basis for further analysis. The aim is to characterize the distribution of the molecules of interest on the cell membrane and to distinguish between randomly distributed and clustered molecule distributions. This is done by comparison with the null hypothesis of randomly distributed molecules and testing for significant deviations. The method for obtaining a p-value is explained in detail in this section.

The resulting image of a two-color SMLM experiment consists of localizations of single fluorophores that are represented by their coordinates on a 2D imaging plane. Hence, the obtained localization map can be interpreted as a spatial point pattern. A short introduction into the theory of spatial point patterns will be given and all the steps needed for the analysis of a point pattern will be described in the following (compare also [54, 55, 56, 57]).

4.3.1   Fundamentals of spatial point pattern analysis

A spatial point pattern consists of a set of objects that are distributed in a given space and characterized by their locations. In our case, the objects are the detected localizations arising from fluorophores bound to the molecules of interest and the given space is the 2D plasma membrane of the cell.

The following important preconditions and assumptions are being made in the further analysis of localization point patterns that may not be neglected when interpreting the results of any analysis.

Assumption of homogeneous experimental conditions. It is assumed that experimental conditions are the same within the whole region of interest.

For a reliable analysis experimental conditions like illumination intensity, labeling efficiency and label ratio need to be the same within the whole observed region. Moreover, membrane curvature has to be taken into account. The plasma membrane is not a flat plane, but a two-dimensional surface that is arranged in three-dimensional space. A high degree of curvature leads to inhomogeneous densities of localizations and thus to heterogeneities, although the molecules might be distributed randomly on the cell membrane. For a reliable analysis of molecule distribution, it is necessary that the cell is well attached to the bottom of the chamber slide without exhibiting too much curvature.

Assumption of points having no spatial extent. Spatial point pattern analysis assumes that the observed objects are points that have no spatial extent and disregards their 2D- or 3D-structure.

If the spatial scale of the objects under investigation is smaller than the scale at which interactions between them occur, this assumption does not impact the outcome of the analysis.

4.3.2 Data type

In order to conduct an appropriate spatial point pattern analysis, we first have to determine the data type of the pattern.

Univariate Point Pattern. An univariate pattern consists of only one type of objects that are characterized by their location in space. When analyzing an univariate point pattern, the question of interest is whether the point process that creates the pattern distributes the objects to all locations within the observed region with equal probability or else, whether there occurs any interaction between the objects like attraction or repulsion.

Bivariate Point Pattern. A bivariate pattern consists of the positions of two distinct types of objects that were created *a priori* by two different processes. In contrast to the case of univariate patterns, the question of interest for bivariate patterns is not the spatial distribution of both of the two composite patterns, but rather possible interactions between them like attraction or repulsion. The concept of bivariate patterns can also be generalized to more than just two composite patterns. If a pattern is composed of more than two individual point processes, it is referred to as multivariate pattern.

Marked Point Pattern. For marked point patterns, one can distinguish between qualitative and quantitative marks. A qualitative mark is a discrete or categorical mark that is assigned to a specific point of the pattern and describes its state, whereas a quantitative mark is a certain (real) number that describes an observed characteristic of a point.

The differences between qualitatively marked point patterns and multivariate point patterns are only subtle. A qualitative marked pattern is created by a single point process that yields an underlying univariate pattern which is subsequently marked by another process that acts *a posteriori* over this given univariate pattern. In contrast, a bivariate or multivariate point pattern is composed of different types of objects that are of that specific type *a priori*. The data type of any point pattern under investigation should be determined with care. There exist pattern analysis tools specific for both univariate and multivariate patterns, however, they will lead to misleading results if applied to the wrong data type.

The pattern that underlies this thesis is the distribution of certain molecules of interest on the cell membrane. This pattern can be interpreted as an univariate point pattern. The molecules are randomly labeled with antibodies carrying specific fluorescent probes that can be of type A or B, respectively. The process of detecting the fluorophores in the microscope and localizing them generates two new point patterns of all the localizations in color channel 1 and 2, respectively. This process is the same for both color channels, however, the subset of molecules carrying the considered label is a different one. Hence, the point pattern should be regarded as a bivariate pattern as opposed to a qualitatively marked pattern.

4.3.3 Summary statistic

Summary statistics characterize the statistical properties and important features of a given point pattern and reveal details about its spatial structure. Common summary statistics for the analysis of point patterns include Ripley's K-function, the pair-correlation function, the spherical contact distribution function and the cumulative distribution function of distances to the nearest neighbor [54]. There exist equivalents for the analysis of bivariate point patterns like the inter-type K-functions and cross-pair correlation functions [55].

An appropriate summary statistic for the analysis of the point pattern created by all the localizations of a single-molecule localization microscopy experiment is the cumulative distribution function $D(r)$ of all distances from the localizations in one color channel to their nearest neighbor among all localizations in the other color channel. It describes the small-scale correlation structure of the given point pattern and gives information about possible local cluster structures and immediate neighborhood relationships. The function $D(r)$ assesses the probability that the neighborhood of a typical point of the pattern is empty. If $D(r) = 0$, no point of the pattern has a neighbor below the scale r. For $D(r) = 1$, all points of the pattern have a nearest neighbor below or at the distance r. Figure 4.5 shows an exemplary pattern of localizations and the corresponding nearest-neighbor distance cumulative distribution function.
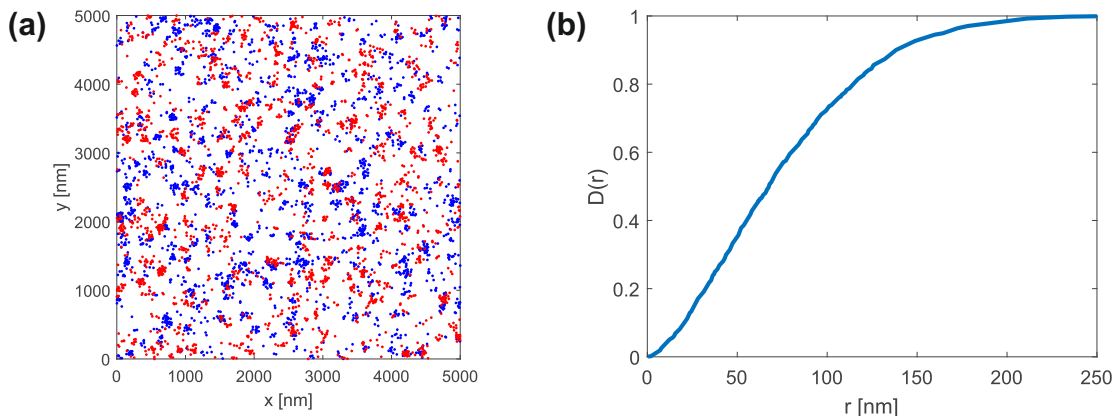

Figure 4.5: **(a)** Localization map for a simulated two-color SMLM experiment. **(b)** Cumulative distribution function of nearest-neighbor distances for data shown in **a**.

4.3.4 Edge bias and edge correction

Many summary statistics show a bias near the edges of the observation region. This bias is especially pronounced at the corners, where only approximately one quarter of all neighboring points lie within the observed region. For the summary statistic of nearest-neighbor distances it might occur that the distance of a point to the nearest border is shorter than the distance to its nearest-neighbor within the observed region. In this case, the actual nearest neighbor might be located outside of the observed region and hence, the nearest-neighbor distance cannot be correctly determined. Therefore, commonly some edge correction method is applied at the edges

in order to minimize the bias.

Minus sampling. For minus sampling only those points are taken into account and analyzed whose distance to the next edge is larger than a given threshold. For nearest neighbor distances, this leads to unbiased estimates of the summary statistic if all those distances are lower or equal to the minus sampling edge. However, a disadvantage of this method is that the information available in the observed point pattern is only partially used, which in turn leads to worse estimates of the summary statistic especially for small numbers of points.

Plus sampling. Plus sampling reconstructs the neighborhood outside of the observed region for points near the edges. One way for such a reconstruction is for example periodic edge correction. The summary statistic is then calculated for all original points within the region of interest and the reconstructed points serve to reduce the bias near the edges.

No edge correction. Without any edge correction, the summary statistic will be biased by points close to the border of the region of interest because they may have unobserved nearest neighbors outside of the observed region. However, if the observation region is large compared to the range of distances between the points, only few points will be affected. Then, the overall bias will probably be rather small and might be neglected.

Without any edge correction, the cumulative distribution function of nearest-neighbor distances $D(r)$ will still be reasonably well approximated if there is a high number of points in the pattern or the pattern is clustered. In this case, nearest-neighbor distances will typically be quite small and only a few points very close to the edges will be affected by a small bias. Moreover, if the pattern under investigation is assessed relative to other realizations of the null model, edge correction may not be necessary because the nearest-neighbor distances of the patterns are all subject to the same bias that cancels out in comparison. Therefore, no edge correction is applied in the further analysis.

4.3.5   Null model

A null model represents a point pattern with a specific spatial structure. It can be used to analyze the data set of a given point pattern and determine whether this point pattern shows any significant spatial structure that does not exist in the null model. The most basic null model that represents the simplest possible randomization of a specific data type is called the fundamental division. It can be used to determine whether the data of a given point pattern contains any spatial structure that can be distinguished from pure stochastic effects. For univariate patterns, the fundamental division is complete spatial randomness (CSR). In general however, the fundamental division does not need to correspond to complete randomization of data, only the characteristics specific to the given data type are randomized. In the case of bivariate patterns, this characteristic is the relationship between the points of different types. The fundamental division represents complete independence between the two component patterns, the structure of which may be arbitrary. Hence, when trying to generate realizations of

the fundamental division for bivariate patterns, the aim is to conserve the univariate structure of the two component patterns, while removing potential interdependence between them. By comparing the given spatial point pattern with realizations of the fundamental division, any attraction or repulsion between points of different types can be detected. [54]

Toroidal shift null model

The toroidal shift null model serves as a nonparametric null model for independence of homogeneous bivariate patterns and was first presented by Lotwick and Silverman in 1982, [58]. It offers a simple way to determine if the component patterns of a given point pattern show any dependence between each other, which is usually quite difficult to be judged visually. The method of the toroidal shift holds one of the two component patterns fixed in space while entirely moving the other pattern by a given random vector on a toroidal geometry. This is done by adding the shift vector to the original coordinates of the data. However, some of the points are moved out of the observation region. Therefore, the shifted pattern subsequently is reassembled by wrapping it on a torus. The acquired new pattern keeps most interpoint distances of the original pattern intact and shows approximately the same univariate spatial structure. However, especially larger structures like clusters are split apart at the region of the borders which may introduce some artifacts. Hence, the pattern generated by a random toroidal shift is not a pure stochastic replicate of the actually observed pattern.

The aim of this thesis is to distinguish between randomly distributed and clustered molecules on the cell membrane. In both cases, the resulting point pattern shows localization clusters due to fluorophore blinking. However, molecular clusters show a characteristic tendency towards shorter nearest-neighbor distances because the molecules within one cluster can be labeled with fluorophores of different types and hence, those fluorophores of different colors are in close proximity to each other. This means that in the case of molecular clusters, there exists interdependence of the localizations from the two different color channels. Therefore, we need to select a null model that breaks apart the spatial relationship between the two point patterns of localizations from color channel 1 and 2, respectively. An appropriate null model for this purpose is the toroidal shift null model described above. The toroidal shift conserves the univariate spatial structure of the two individual point patterns while breaking apart any possible spatial relationship between them. An example of a toroidal shift applied to simulated data is shown in figure 4.6.

4.3.6 Comparison of data and null model

After the acquisition of data from a two-color single-molecule experiment or simulation, this data needs to be compared to the null model. Therefore, we need to generate controls that are realizations of this null model. The objective of these controls is to determine whether the test statistic calculated for the observed data is within the range of stochastic fluctuations around a theoretically expected value that are produced by the null model or whether it falls outside
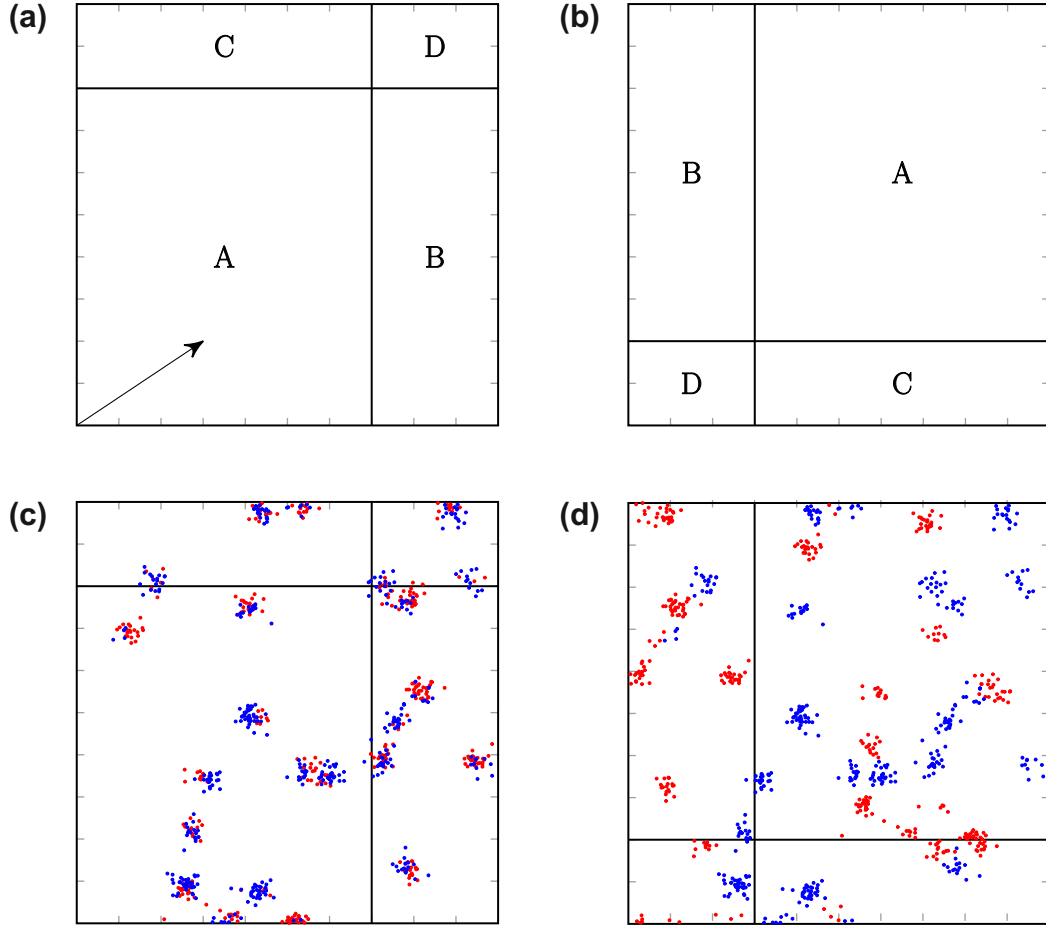
Figure 4.6: Toroidal shift. **(a)** Original region of interest. The arrow indicates the vector of shift. After shifting the pattern, the areas B, C and D lie outside of the observed region. Therefore, the pattern is reassembled following a toroidal geometry, resulting in **(b)**. Exemplary, a toroidal shift is applied to data obtained from a two-color SMLM experiment. Original data is shown in **(c)**. After applying a toroidal shift to all localizations from color channel 1 (indicated with red points) the pattern is reassembled, yielding the pattern shown in **(d)**.

of this range. [54] A higher number of controls leads to more reliable results, however, this advantage comes with the disadvantage of higher computational expenses. For the analysis of the simulation results and experiments (see sections 5.1 and 5.2), the number of controls used was $n = 99$. The controls are generated by applying random toroidal shifts to the localizations of color channel 1 while the localizations of color channel 2 are kept at their original positions. A toroidal shift is realized by adding a random vector of shift $(x_{\text{shift}}, y_{\text{shift}})$ to the localization positions:

$$(\tilde{x}, \tilde{y}) = (x, y) + (x_{\text{shift}}, y_{\text{shift}}).$$

The values x_{shift} and y_{shift} for the shift in x- and y-direction are drawn from a uniform distribution on the intervals $I_x = [s_{\min}, a_x - s_{\min}]$ and $I_y = [s_{\min}, a_y - s_{\min}]$, respectively, where a_x and a_y are the side lengths of the region of interest and $s_{\min}$ is the value of the minimal shift which

is set in order to consistently split apart any interdependences between the two component patterns. For the analysis of simulated and experimental data in this thesis, the value of minimal shift was set as $s_{\min} = 100\,\text{nm}$. In order to assure that all localizations lie within the region of interest, resulting x- and y-positions are taken modulo a_x and a_y, respectively.

As a next step, all nearest-neighbor distances of the data from channel 1 to their nearest-neighbor localization in channel 2 have to be determined. This has to be done for the original (unshifted) data, as well as for all shifted data from channel 1 that serve as the controls. From the calculated distances, the cumulative distribution functions of nearest-neighbor distances can be determined as

$$F_D(d) = \mathbb{P}(D \leq d) = \int_0^d f(r)dr, \tag{4.4}$$

where $f(r)$ is the probability distribution function of nearest-neighbor distances. The cumulative nearest-neighbor distribution function $F_i(x)$ is calculated for the original data ($i = 0$) and each control ($i = 1, \dots, n$). Figure 4.7 shows exemplary results for simulated data for two cases of randomly distributed and clustered molecules, respectively.
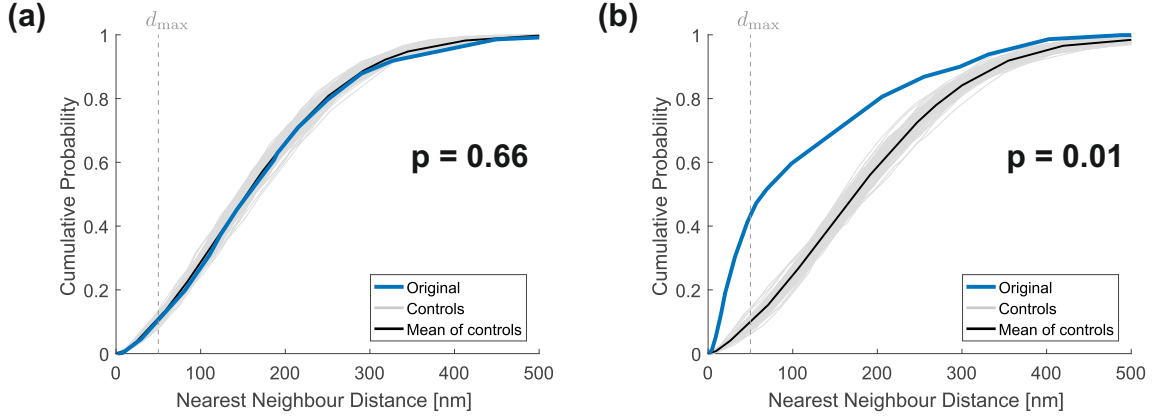

Figure 4.7: Cumulative distribution functions (CDFs) of nearest-neighbor distances for original and control data in the case of (a) randomly distributed or (b) clustered molecules on the cell membrane. Gray lines show the CDFs for 99 controls generated by applying random toroidal shifts to the data. The black line shows the mean of all control CDFs, the blue line shows the CDF of nearest-neighbor distances for the original data.

The cumulative distribution function of nearest-neighbor distances under the null hypothesis of randomly distributed molecules is not known analytically. However, from all obtained controls we can calculate a mean cumulative distribution function as

$$F(x) = \frac{1}{n} \sum_{i=1}^{n} F_i(x). \tag{4.5}$$

The obtained function $F(x)$ is an estimate for the cumulative distribution function under the null hypothesis and is used as its surrogate.

In order to be able to easily compare the obtained test statistics for the original and control

data, we calculate the goodness of fit between the cumulative nearest-neighbor distance distribution functions $F_i(x)$ of the original (observed) data and the controls (shifted data) to the mean cumulative distribution function $F(x)$ given in equation (4.5). Thereby, the functional test statistic $F_i(x)$ of the nearest-neighbor distances is transformed into a single value s_i that represents the deviation of the summary statistic from the test statistic expected under the null model:

$$s_i = \int_0^{d_{\max}} \left(F_i(x) - F(x) \right) dx \qquad \text{for } i = 0, ..., n \,.$$ (4.6)

The range of distances $(0, d_{\max})$ over which the integral is calculated should be chosen with care (compare [54]). Because we are interested in deviations from the null model at the scale of oligomerization or molecular clusters, we set $d_{\max} = 50\,\text{nm}$.

The question of interest is whether the considered set of localizations arises from randomly distributed molecules on the cell membrane (null hypothesis) or shows any kind of spatial structure like molecular clustering (alternative hypothesis). We obtain an estimation of the p-value for this test decision by

$$p = \frac{1}{n+1} \sum_{i=0}^{n} H(s_i - s_0) \,,$$ (4.7)

where $H(x)$ is the Heaviside step function defined as

$$H(x) = \begin{cases} 0, & \text{for } x < 0, \\ 1, & \text{for } x \geq 0. \end{cases}$$ (4.8)

The sum in equation (4.7) effectively calculates the rank of the test statistic s_0 of the original data among all the controls.

The null hypothesis of a random distribution of molecules of interest on the cell membrane is rejected if the p-value is below the chosen level of significance γ. If the p-value is greater than γ, the null hypothesis cannot be rejected and it has to be assumed that the molecules are randomly distributed. The level of significance γ usually is chosen to be $\gamma = 0.01$ or $\gamma = 0.05$.

When interpreting the results of the analysis, it should always be taken into account that from the obtained p-value alone one cannot infer much about the kind of deviations between the analyzed data and the null model. Therefore, in addition one always should inspect the cumulative nearest-neighbor distribution function of the original data with respect to the range of stochastic fluctuations generated by the controls. Further details regarding hypothesis testing in the above described way can be found in the literature [56, 59, 60].

Chapter 5

Results

In single-molecule localization microscopy, repeated observations of single fluorophores lead to clustered localizations. A novel analytical method for distinguishing clustering artifacts from real molecular clustering is suggested in this thesis and described in detail in section 4.3. Targeting the molecule of interest with differently labeled antibodies allows for the calculation of distribution functions of nearest-neighbor distances between the localizations of both color channels. Random toroidal shifts of the data from one color channel provide realizations of the null hypothesis of an underlying random distribution of molecules. Those controls allow for statistical significance tests and estimation of p-values. If the obtained p-value is smaller than or equal to the level of significance γ, usually chosen as $\gamma = 0.01$ or $\gamma = 0.05$, we reject the null hypothesis of randomly distributed molecules and assume that the distribution of molecules on the cell membrane shows some kind of clustering. Otherwise, for p-values greater than the level of significance, we stay with the null hypothesis of randomly distributed molecules.

In order to evaluate the performance of the method, its sensitivity and specificity can be investigated. These terms are defined as

$$\text{sensitivity} = \frac{\text{true positives}}{\text{true positives} + \text{false negatives}}$$

and

$$\text{specificity} = \frac{\text{true negatives}}{\text{false positives} + \text{true negatives}} \;.$$

For achieving a good performance, it is important that the method has a high sensitivity on the one hand, but also a high specificity on the other hand. A high sensitivity means that the method is able to correctly identify clustered molecules and that there are only a low number of cases of clustered molecules that are incorrectly identified as being randomly distributed. For a high specificity, randomly distributed molecules must not be incorrectly identified as clustered.

The robustness of the proposed method was evaluated with Monte Carlo simulations (see also section 4.1). Moreover, the performance of the method in real experimental conditions was tested on monomeric, dimeric, trimeric and tetrameric molecules (see also section 4.2). The results are presented in the following sections.

5.1 Simulations

In order to investigate the influence of various experimental parameters on sensitivity and specificity of the method, simulations with a variation of different parameters like labeling efficiency, labeling ratio, blinking behavior and background fluorescence were performed. Various scenarios of randomly distributed molecules, oligomerization and clustering were considered. For each parameter set $N = 1000$ simulations were performed and the obtained localization maps analyzed as described in section 4.3. Briefly, 99 controls were generated by toroidal shifts of the simulated data of color channel 1. P-values were obtained by comparing the nearest-neighbor distance distributions of the original data and all controls. For an overview of all input parameters for the simulations refer to the appendix A.1.

5.1.1 Random distributions

In the case of randomly distributed molecules on the cell membrane, which is the null hypothesis of the statistical test, the distribution of p-values should be uniform on the interval $I = [0, 1]$.

Simulations were performed using different blinking statistics, molecule numbers, labeling efficiency, label ratio, numbers of background localizations and numbers of unspecifically bound labels. Figure 5.2 shows an exemplary histogram of p-values and cumulative distribution functions of p-values for all simulated parameter sets. It can be seen that the distribution of p-values is approximately uniform in all cases. This indicates a low number of false positives and hence, a high specificity of the test.
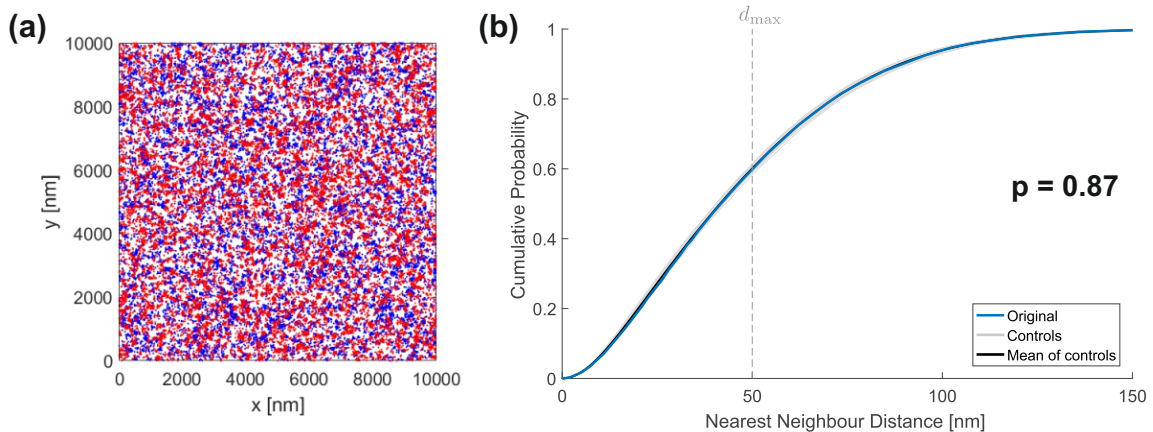

Figure 5.1: Exemplary data of simulated randomly distributed molecules. **(a)** Region of interest. Localizations from color channel 1 and 2 indicated with red and blue marks, respectively. **(b)** Cumulative distribution functions of nearest-neighbor distances for original data (blue) and controls (gray).
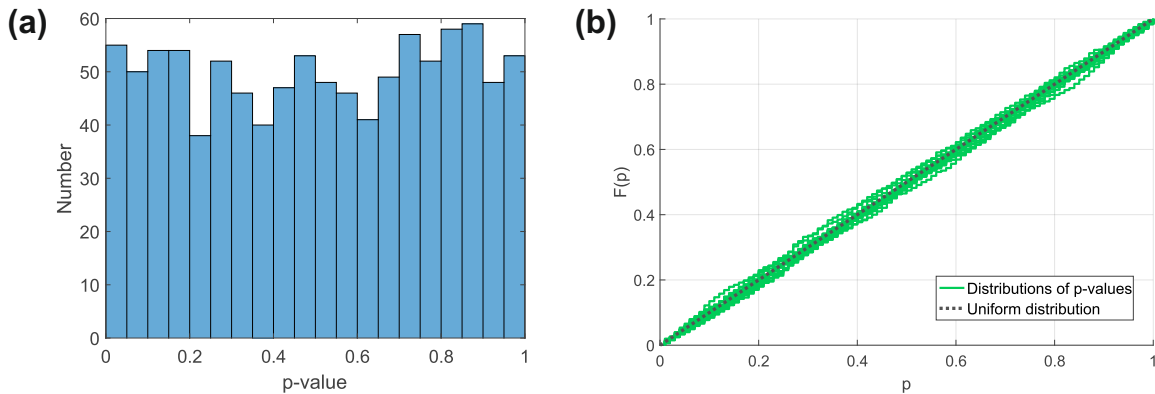
Figure 5.2: P-values for randomly distributed molecules (for $N = 1000$ simulations per parameter set). An overview of all used parameters is given in the appendix A.1. **(a)** Exemplary histogram of p-values. **(b)** Cumulative distribution functions (CDFs) of p-value distributions for various sets of parameters. The gray line indicates the CDF of a uniform distribution.

5.1.2 Oligomerization and clustering

The sensitivity of the method was evaluated with various scenarios of oligomerization and clustering. The results for different sets of parameters are presented in the following. For investigating the influence of a specific parameter on the performance of the method, all parameters except one were kept fixed on a certain baseline value while varying the parameter in question over a certain range. All simulations presented below were performed based on the simulation parameters of parameter set 1, 2, or 3, given in a table in appendix A.1. Parameter set 1 simulated a region of interest on the cell membrane with all proteins present as dimers and good experimental conditions like high labeling efficiency and a low number of localizations from background signals or unspecifically bound labels. The parameter values of parameter set 2 were chosen to represent an experiment with only 30 percent of molecules in a dimeric state and worse experimental conditions, such as lower labeling efficiency and higher number of background localizations or localizations from unspecifically bound labels. Figure 5.3 shows exemplary results for both of the parameter sets. Parameter set 3 represents even worse experimental conditions at only 40 percent labeling efficiency and a monomer fraction of 0.8.

Blinking Statistics

The blinking of fluorophores was simulated using the experimentally measured blinking statistics of PS-CFP2, Alexa647-KT3 and Alexa647-H57 (see section 4.1.1). The influence of the blinking distribution on the performance of the method was investigated using the baseline values of parameter set 2. The results are presented as percentage of correctly identified clustering in table 5.1. Those simulations that used the blinking statistic of Alexa647-H57 performed the worst in the detection of clustering. This is probably due to the fact that the distribution of number of blinks of Alexa647-H57 has a long tail and includes numbers of blinks up to 1572.
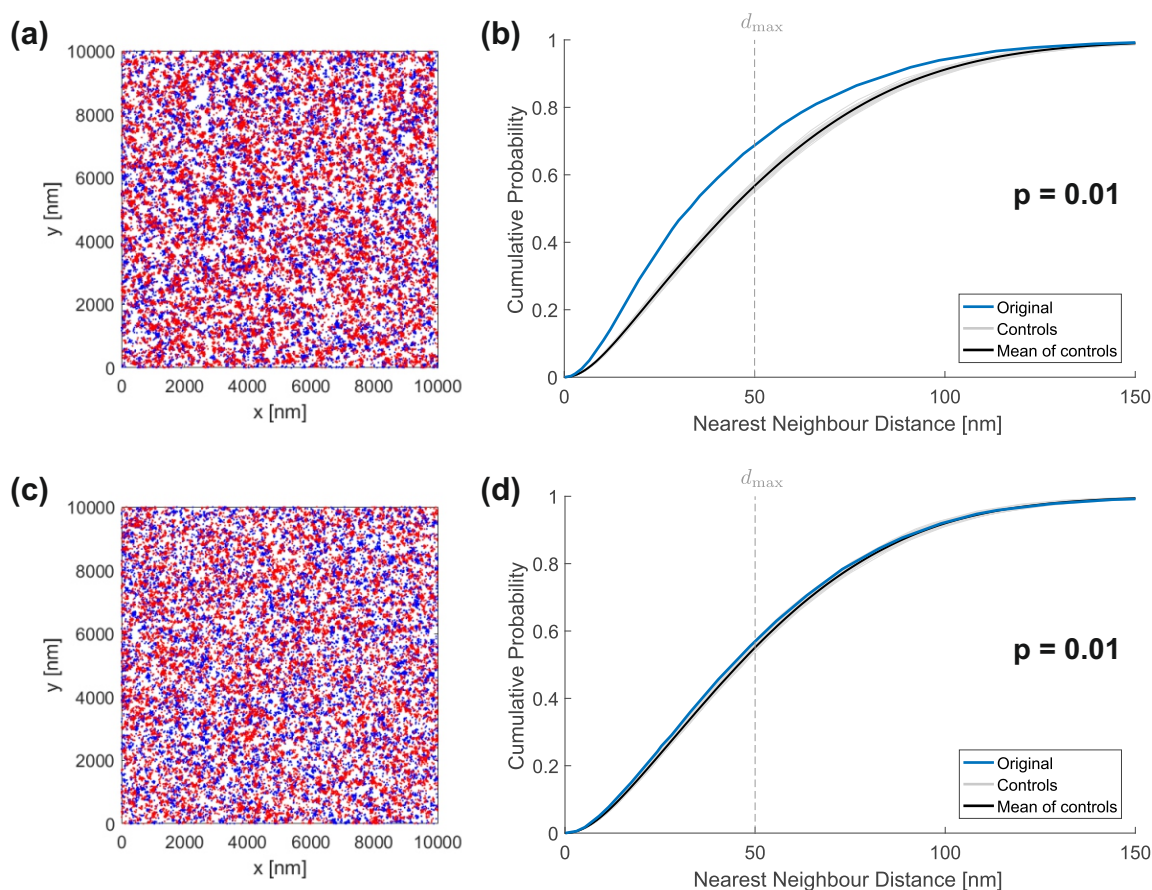
Figure 5.3: Exemplary data of simulated clustered molecules. **(a, c)** Regions of interest. Localizations from color channel 1 and 2 indicated with red and blue marks, respectively. **(c, d)** Cumulative distribution functions of nearest-neighbor distances for original data (blue) and controls (gray). Simulations were performed with parameter set 1 (**a** and **b**) and parameter set 2 (**c** and **d**). In both cases, the obtained p-value is $p = 0.01$.

Multiple localizations of the same molecule due to blinking are statistically dependent and will lead to approximately the same nearest-neighbor distances. Hence, a few outliers with a very high number of blinks put a high weight on the corresponding small range of nearest-neighbor distances and hence, may distort the overall statistics.

Molecule Number

The influence of the number of molecules of interest present on the cell membrane was investigated with simulations performed based on parameter set 2. The amount of correctly identified clustering is shown in figure 5.4. Higher density of molecules led to better detection of oligomerization. In general, this result is supported by the fact that a larger number of observations leads to more reliable statistics. However, in this case it should be kept in mind that only the number of molecules was varied and all other parameters, including background localizations and unspecifically bound labels, stayed fixed. Hence, the ratio of localizations from real molecules to other localizations increased with a higher number of molecules, which

		Percentage detected	
Label A	Label B	$\gamma = 0.01$	$\gamma = 0.05$
Alexa647-KT3	Alexa647-KT3	82.5	96.9
PS-CFP2	PS-CFP2	69.4	92.1
Alexa647-H57	Alexa647-H57	54.5	83.5
Alexa647-KT3	PS-CFP2	77.5	95.5
PS-CFP2	Alexa647-KT3	76.3	94.7
Alexa647-KT3	Alexa647-H57	75.6	94.0
Alexa647-H57	Alexa647-KT3	67.4	91.5
PS-CFP2	Alexa647-H57	70.6	92.4
Alexa647-H57	PS-CFP2	64.7	87.2

Table 5.1: Influence of blinking behavior of labels A and B on the sensitivity of the method given in percentage of correctly identified clustering.

may be an additional reason for the better performance of the method. Another point to take into consideration is that with higher density of molecules, the distances to nearest neighbors decrease. If all nearest-neighbor distances are below the positional accuracy, nearest-neighbor distributions of randomly distributed molecules and oligomerization will not be distinguishable anymore. However, such a high density of molecules is experimentally unlikely.
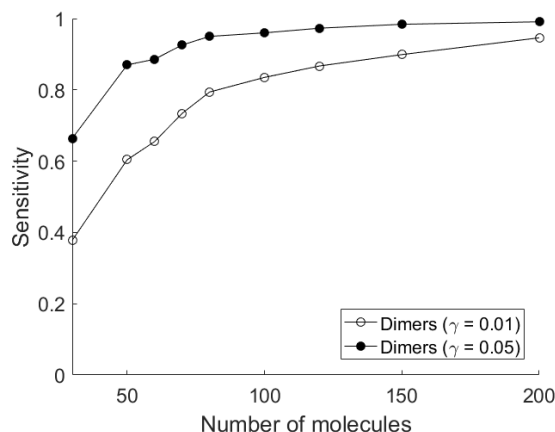

Figure 5.4: Impact of number of molecules on sensitivity.

Labeling Efficiency and Label Ratio

In ideal experimental conditions all molecules would carry a label, corresponding to a labeling efficiency of 100 percent, and the amount of labels of type A and type B would be equal, corresponding to a label ratio of 50:50. The effect of deviations from this ideal case was evaluated by simulations performed based on parameter sets 1 and 2, respectively. Results are presented in figure 5.5.

In practice, labeling efficiency is strongly dependent on the specific molecule of interest and the label type and will hardly reach labeling of all molecules. The lower the labeling efficiency, the less oligomers will be labeled with fluorophores of two different colors. Therefore, those

oligomers cannot be detected, which leads to overall worse detection of oligomerization.

The effect of label ratio is conceptually the same. If there is a high amount of one type of fluorophore, but only a small amount of the other type, only a little number of oligomers will carry labels of different colors, hence, impeding the detection of oligomerization.
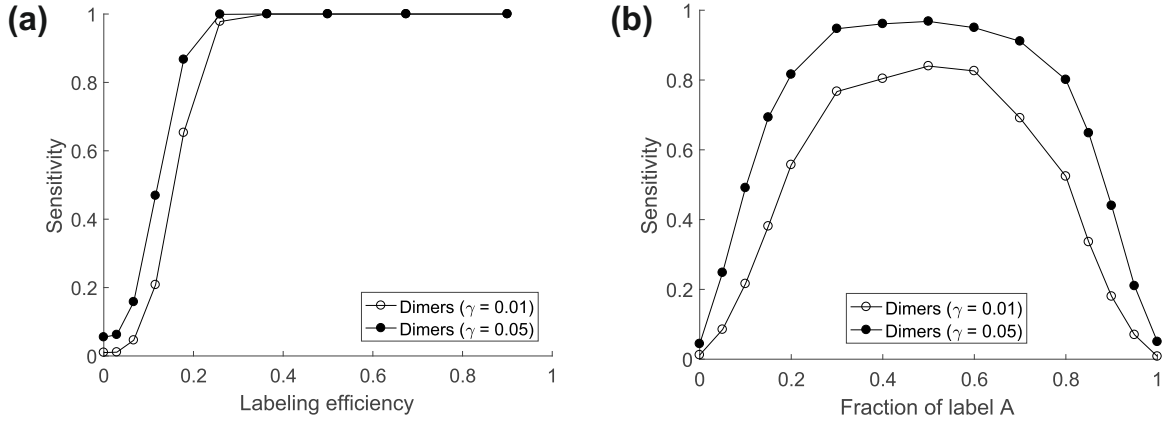

Figure 5.5: Impact of **(a)** labeling efficiency and **(b)** label ratio on sensitivity. Labeling efficiency that is too low impedes the detection of oligomerization. The sensitivity of the method is rather unaffected by slight deviations from a 50:50 label ratio.

Background and Unspecifically Bound Labels

Background localizations and localizations from unspecifically bound labels constitute additional localizations that do not arise from fluorophores bound to molecules of interest. In simulations, it was assumed that localizations belonging to background and unspecifically bound labels, respectively, both show a random distribution on the region of interest. By adding these localizations, the localizations from a clustered pattern of molecules of interest are combined with localizations from a random pattern. Hence, the effect of clustering in the overall statistics is reduced. Therefore, both background and unspecifically bound labels might decrease the sensitivity of the method. However, it can be inferred form figure 5.6 that just small numbers of background localizations and unspecifically bound labels do not have a very high impact on correct identification of oligomerization. The sharper decline in sensitivity for unspecifically bound labels compared to background localizations is due to the fact that any background signal is simulated as one localization only, whereas unspecifically bound labels show blinking and therefore have more effect on the nearest-neighbor distance statistics.
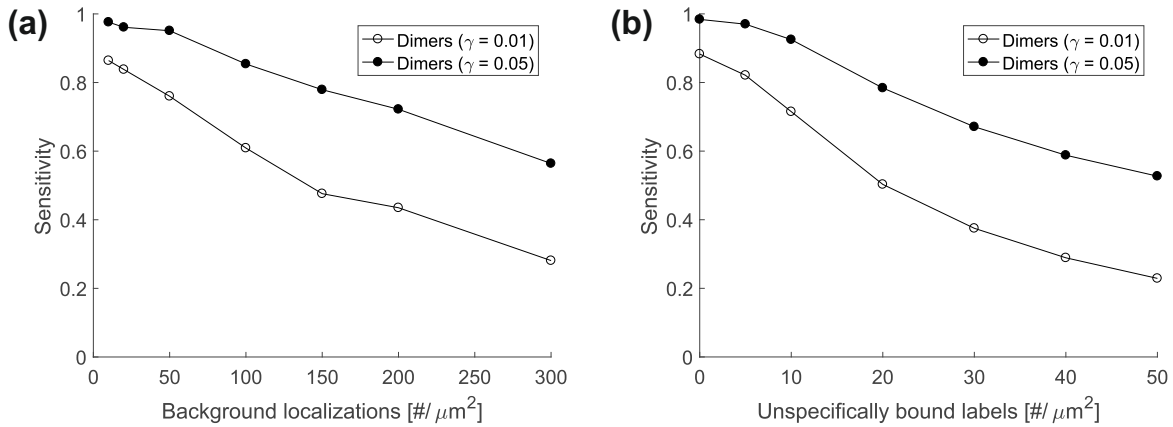
Figure 5.6: Impact of **(a)** background localizations and **(b)** unspecifically bound labels on sensitivity. A high number of background localizations or unspecifically bound labels reduces the sensitivity of the method.

Monomer fraction

The sensitivity of the method for cases in which only a part of the molecules of interest is present in an oligomeric state was evaluated with simulations based on parameter set 1. In general, a higher monomer fraction will reduce the spatial information from oligomerization and hence, impact the ability of the method to detect oligomerization. Figure 5.7 shows that with good experimental conditions, including a high labeling efficiency of 95 percent, even small dimer fractions of around 20 percent could be detected in simulations. However, if some experimental parameters show less desirable values, the sensitivity of the method towards such low dimer fractions will drop.
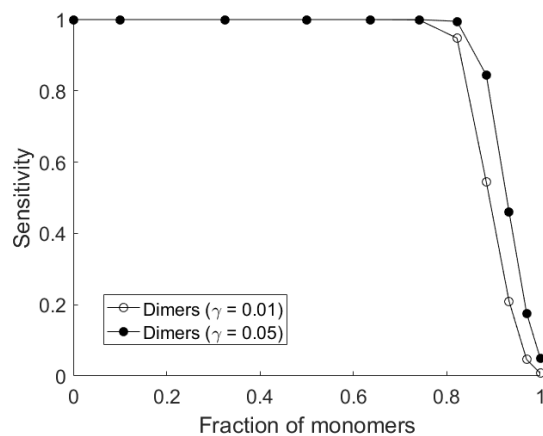

Figure 5.7: Impact of monomer fraction on sensitivity. Under good experimental conditions even a small dimer fraction of 20 percent can be reliably detected.

47

Stage Drift

While performing a microscopy experiment, some drift of the microscope stage may occur due to temperature variations or mechanical instabilities. The impact of stage drift on the results of clustering analysis was evaluated with simulations based on parameter set 2. For overall drift of the stage of less than 100 nm throughout all of the 10000 recorded frames, oligomerization could still be correctly identified. For higher values of overall drift, the sensitivity of the method declined.
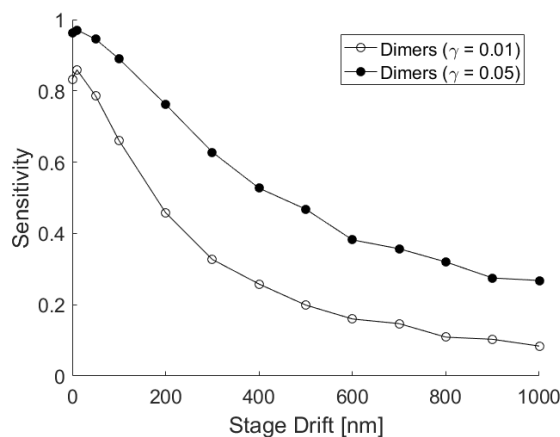

Figure 5.8: Impact of stage drift on sensitivity. Stage drift reduces the sensitivity of the method.

Chromatic Aberration

Due to the dependence of refractive indices of lenses on the wavelength of light, light of different wavelengths is focused at different positions in the focal plane. This leads to radial distortion of the image of one color channel with magnification increasing radially. The further away from the optical axis, the more the nearest-neighbor distances will deviate from their real value and localizations from molecules within the same molecular cluster but labeled with different fluorophores will be pulled apart. Figure 5.9 shows how the sensitivity of the method is affected by chromatic aberration. The amount of chromatic aberration is given by the value of deviation in nm per μm off the optical axis, which was simulated to be in the center of the region of interest. In part, chromatic aberration can be corrected by the use of fiducial markers and appropriate post-processing of SMLM data.
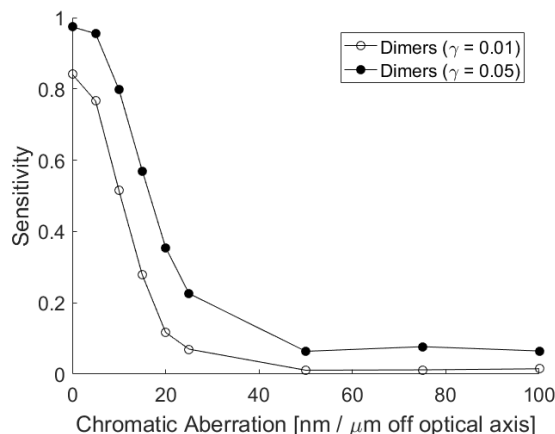
Figure 5.9: Impact of chromatic aberration on sensitivity. Sensitivity decreases with increasing distortions due to chromatic aberration.

Degree of Oligomerization

The degree of oligomerization plays an important role for the sensitivity of the method. The higher the degree of oligomerization, the higher the probability that an oligomer is labeled with fluorophores of both types and hence, can be detected as oligomer. Therefore, the method shows higher sensitivity for oligomers of higher degrees as shown in figure 5.10. For the given parameters of parameter set 3, not even half of the cases of simulated dimers were correctly identified, whereas for simulations of tetramers, oligomerization was correctly identified in nearly all cases.
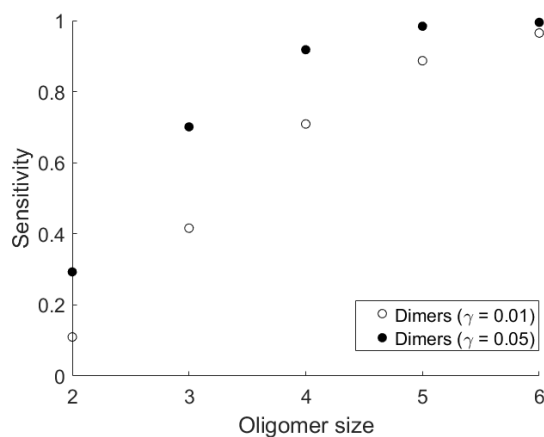

Figure 5.10: Impact of degree of oligomerization on sensitivity. Sensitivity increases with higher degree of oligomerization.

5.2 Experiments

Experiments were performed on HeLa cells, transiently transfected with 1xSNAP-GPI, 2xSNAP-GPI, 3xSNAP-GPI or 4xSNAP-GPI. Cells were colabeled with SNAP-AF647 and SNAP-AF488, fixed and imaged using dSTORM (see section 4.2). 10000 frames per color channel were recorded. Localization maps were obtained from the detected intensities on the CCD camera using ThunderSTORM. The resulting single molecule positions were analyzed as described in section 4.3. Briefly, 99 controls were generated by applying random toroidal shifts to the data of color channel 1 (localizations of Alexa Fluor 647). Nearest-neighbor distance distributions were calculated for the original data and all controls. Resulting distributions were compared in order to obtain p-value estimations for the null hypothesis of randomly distributed molecules and the alternative hypothesis of clustering or oligomerization.

Figure 5.11 shows exemplary region of interests on a cell membrane and corresponding cumulative distribution functions of nearest-neighbor distances for experimental data acquired from a cell expressing monomeric SNAP-GPI and tetrameric SNAP-GPI, respectively. The obtained p-value for monomeric 1xSNAP-GPI was $p = 0.68$, hence, the molecule distribution
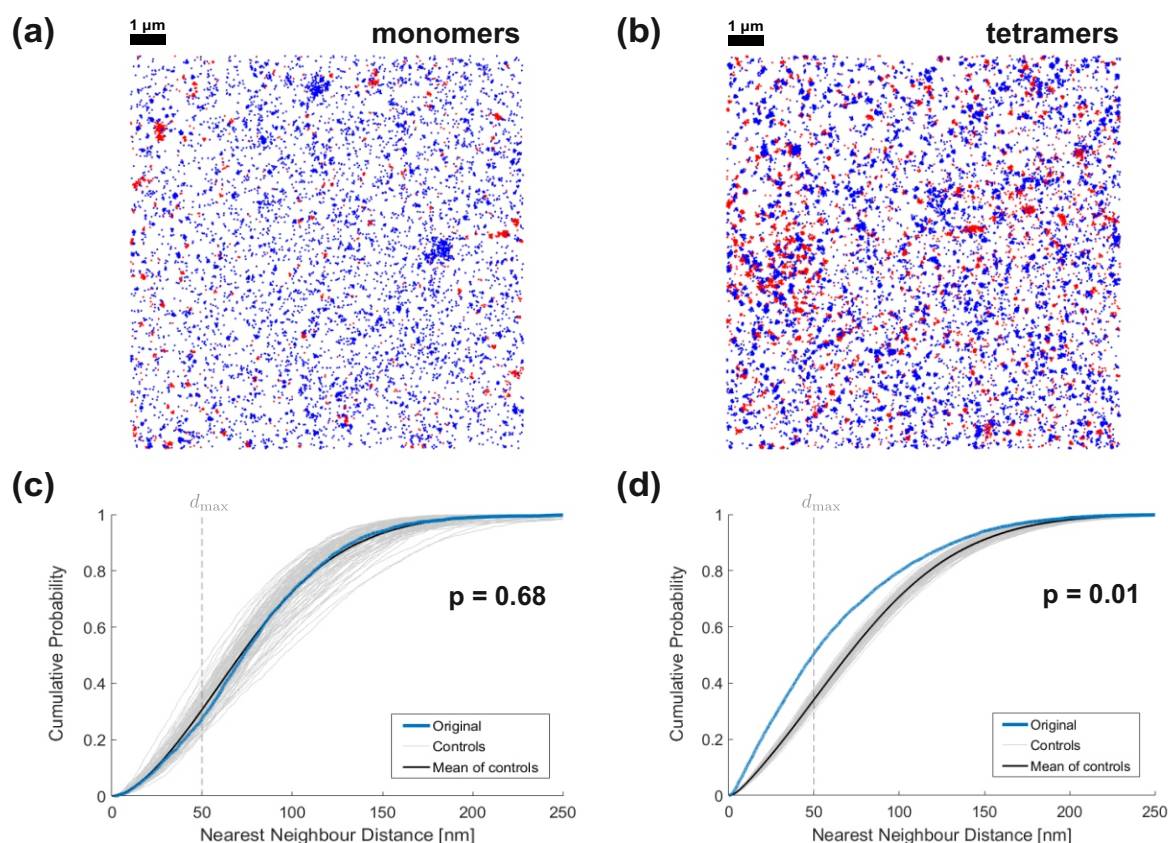

Figure 5.11: Exemplary ROIs **(a, b)** and CDFs **(c, d)** of experimental data from a cell transfected with monomeric 1xSNAP-GPI **(a, c)** and tetrameric 4xSNAP-GPI **(b, d)**, respectively. Positions of localizations from color channel 1 and 2 are indicated with red and blue marks, respectively. Obtained p-values were $p=0.68$ for monomeric and $p=0.01$ for tetrameric SNAP-GPI.

was correctly identified as random. For tetrameric 4xSNAP-GPI, the obtained p-value was $p = 0.01$. Hence, the molecule distribution was correctly identified as clustered.

Within four experimental days, images of 20 cells expressing monomeric 1xSNAP-GPI, 20 cells expressing dimeric 2xSNAP-GPI, 20 cells expressing trimeric 3xSNAP-GPI and 15 cells expressing tetrameric 4xSNAP-GPI were recorded. All data was analyzed and the results are summarized in the histograms of obtained p-values shown in figure 5.12. The histogram of p-values for monomeric 1xSNAP-GPI shows a near uniform distribution. The higher the degree of oligomerization, the more cases are detected as being clustered. Tetramers could be reliably detected under the given experimental conditions.
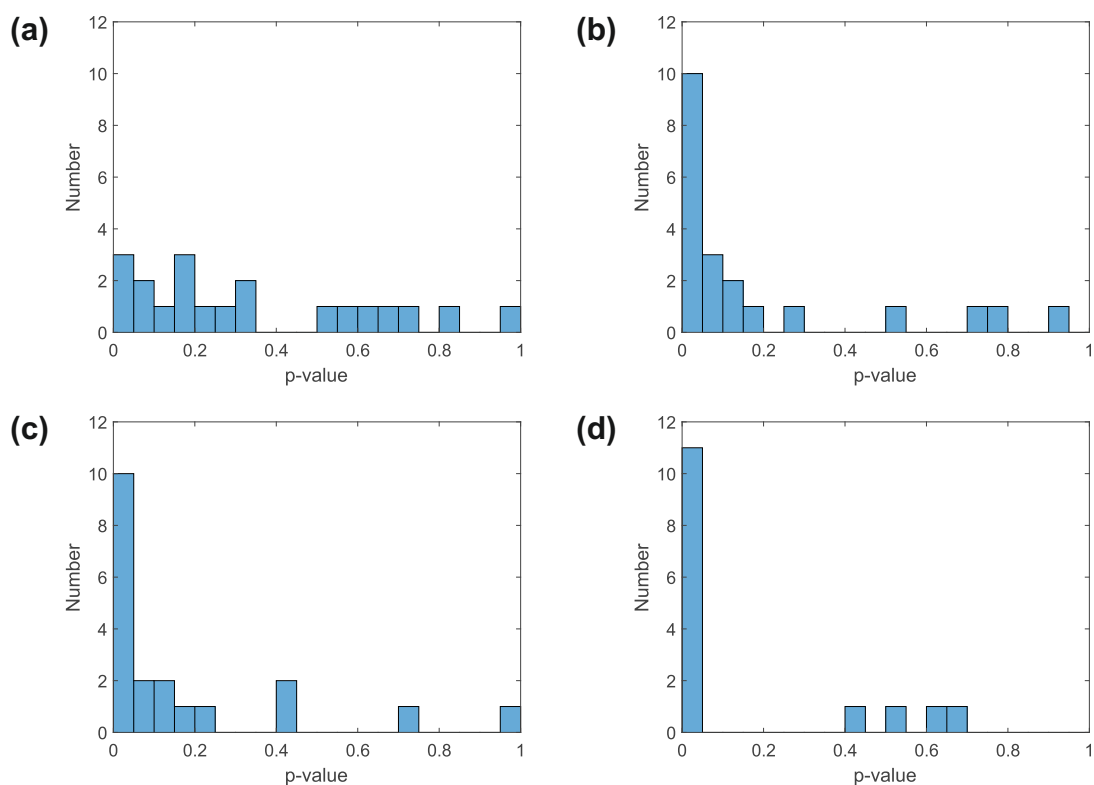

Figure 5.12: Histograms of p-values for imaged cells transfected with **(a)** monomeric 1xSNAP-GPI, **(b)** dimeric 2xSNAP-GPI, **(c)** trimeric 3xSNAP-GPI and **(d)** tetrameric 4xSNAP-GPI.

Chapter 6

Discussion

Single-molecule-localization microscopy methods are based on the stochastic activation of fluorophores to achieve images with a resolution below the diffraction limit. However, repeated observations of single fluorophores lead to clustered localizations, which may be misinterpreted as molecular clustering at the nanoscale. This may lead to wrong inferences about cellular structure and behavior, distorting the results from those areas of research. This thesis suggests a novel analytical approach to distinguish localization clusters from real molecular clustering. Targeting the same protein species with antibodies labeled with two different fluorophores showing distinct emission spectra allows for the calculation of nearest-neighbor distance distribution functions between localizations from both color channels. Real Molecular clusters exhibit a strong tendency towards shorter distances. This characteristic can be used for estimating a p-value for the null hypothesis of randomly distributed molecules and the alternative hypothesis of clustered molecules. Applying random toroidal shifts to the data of one color channel breaks correlations between the two channels and provides realizations of the null hypothesis. P-values are obtained by comparing the original data with the controls. The method was tested with simulations of both clustered and randomly distributed molecules on the cell membrane with varying labeling efficiency, labeling ratio and blinking behavior. Even small dimer fractions of 20 percent could be detected in simulations. Experiments were performed on HeLa cells, transiently transfected with 1xSNAP-GPI, 2xSNAP-GPI, 3xSNAP-GPI or 4xSNAP-GPI, and colabeled with SNAP-AF647 and SNAP-AF488. Tetramers could be reliably detected under experimental conditions.

6.1 Method

6.1.1 Assumption of homogeneous experimental conditions

An important assumption of the method presented in this thesis are homogeneous experimental conditions throughout the whole region of interest (see section 4.3). Experimental conditions and any other influences need to be the same within the whole observed region. This concerns for example illumination intensity, labeling efficiency and label ratio. Moreover, the cell needs

to be well attached to the bottom of the chamber slide. If experimental conditions vary within the observation region, the point pattern of localizations is not invariant under translation and toroidal shifts will not generate reliable surrogates for realizations of the null hypothesis. Then, p-values might be low due to experimental heterogeneities and may produce misleading results regarding the distribution of molecules of interest.

Other kinds of heterogeneities that can be present in a cell, like endocytosed vesicles or exclusion zones, may also lead to small p-values. This should be taken into account when interpreting the results of the analysis.

6.1.2 Estimation of p-value

The described method is not a rigorous statistical test, but generates realizations of the null hypothesis for obtaining an estimation of the desired p-value. The precision of the p-value depends on the numbers of generated controls. In the case of 99 controls, the p-value can only take on values from $p = 0.01$ to $p = 1$ in steps of 0.01. If more controls are generated, the p-value will be more precise. However, this comes with a high increase in computational costs especially for high numbers of localizations.

For obtaining the controls, random toroidal shifts are applied to all localizations from one color channel. The toroidal shifts conserve most of the spatial structure of the pattern, but tear apart some of the localization clusters. Therefore, the resulting point pattern is not an ideal realization of the null hypothesis and the resulting statistics may be affected by a small bias. However, this bias is negligible for sufficiently large regions of interest.

6.1.3 Cluster radius

There can be various forms of non-random distributions of molecules on the cell membrane. For example, several monomer units can be bound together by non-covalent interactions forming an oligomer. In addition, molecules can group together and aggregate, forming a nanocluster or a cluster at a larger length scale. The presented method using two-color fluorescence microscopy is well suited for the detection of oligomerization and nanoclusters at a length scale of the positional accuracy. For the detection of clustering at larger scales, the value of $d_{\max}$ (see equation (4.6)) should be adjusted according to the desired cluster size.

6.1.4 Qualitative method

The suggested method uses two-color fluorescence microscopy for investigating the distribution of molecules of interest on the cell membrane. Toroidal shifts of the data generate realizations of the null hypothesis of randomly distributed molecules. The distribution of molecules from the original data can be determined by comparing its nearest-neighbor distance distribution to those of the controls. Hereby, the method can distinguish between randomly distributed molecules and molecular clustering. However, it does not offer any possibility to determine whether molecules of interest are present in dimers, trimers etc. or whether there is some other

form of nanoclustering. Hence, the method only gives a qualitative assertion about the deviation from a pure random distribution of molecules on the cell membrane.

6.1.5 Blinking behavior

The presented method does not require any knowledge of the blinking behavior of the fluorophores used in the experiment. This is an apparent advantage as exact blinking statistics are often unknown. The number of detections of a single molecule does not only depend on the number of times a single fluorophore switches between its bright and dark state throughout image acquisition, but also on the number of fluorophores that can be bound to a single molecule of interest.

As shown in section 5.1 the blinking behavior has a rather small impact on the results. The only factor that might impede sensitivity and specificity of the method are outliers that show a very high number of blinks as they are statistically dependent and bias the overall statistics of nearest-neighbor distances. Therefore, it is advised to ensure that this is not the case for the used fluorescent label.

6.1.6 Robustness

A further advantage of the method is that it is robust with regard to several experimental parameters. For example, the number of labels of type A does not need to be exactly equal to the number of labels of type B. Label ratios that slightly differ from this ideal condition do not heavily impede the sensitivity of the method. The higher the degree of oligomerization, the more robust is the method. Therefore, high degrees of oligomerization are still detected also under non-ideal experimental conditions.

6.2 Simulations

6.2.1 Fixation

When studying the distribution of a molecule of interest in the cell membrane, the cell usually is chemically fixed in order to prevent any rearrangement of molecules during image acquisition. However, chemical fixation is usually not sufficient to completely immobilize all molecules that constitute the cell membrane and there might be some residual diffusion of molecules [24]. All simulations performed in this thesis assumed that molecules are perfectly fixed and neglected any residual diffusion due to reasons of computational costs. However, it is assumed that low values of diffusion do not have a severe impact on the outcome of the method.

6.2.2 Parameters

The influence of various parameters on the performance of the method was investigated and is presented in section 5.1. For this, all but one parameters were kept at a fixed value while the remaining parameter was varied over a certain range of values. This gave an insight into how

the sensitivity of the method is influenced by each parameter. However, these findings are more qualitative than quantitative. Exact values of a certain parameter for which the sensitivity falls below a given threshold are heavily influenced by all other parameters of experimental conditions. For example, unspecifically bound labels will not particularly affect sensitivity if labeling efficiency is high and monomer fraction is low. In the case of low labeling efficiency and high monomer fraction however, we find that unspecifically bound labels further reduce sensitivity. Thus, for the assessment of whether experimental conditions are acceptable for carrying out the experiment and data analysis, all parameters should be considered together.

6.3 Experiments

Under the conditions of the performed experiments the tetrameric 4xSNAP-GPI could be reliably detected. The sensitivity of the method to the dimeric 2xSNAP-GPI and tetrameric 3xSNAP-GPI was lower. These experimental results coincide with the findings that higher degrees of oligomerization can be detected more reliably (compare figure 5.10). The detection of lower degrees of oligomerization was most likely impeded by the low labeling efficiency of the SNAP-constructs.

Ideally, the histogram of p-values for monomeric 1xSNAP-GPI should follow a uniform distribution. However, testing the obtained p-values with a one-sample Kolmogorov-Smirnov test against a uniform distribution on the interval $I = [0, 1]$ results in a p-value of $p = 0.025$. This indicates that there actually is some sort of inhomogeneity in the cells that could be caused by various factors further explained previously in section 6.1.1. However, although not completely uniform, the distribution of p-values for monomers still shows a distinct difference to the distribution of p-values obtained for cells expressing dimers, trimers or tetramers. For comparison of the distributions between the results for monomers and higher degrees of oligomerization, a two-sample Kolmogorov-Smirnov test was carried out. The p-values obtained from this test were $p = 0.042$ between the results for monomers and dimers, $p = 0.023$ between monomers and trimers and $p = 0.001$ between monomers and tetramers. Hence, there is a significant difference between the outcome of the experiments for monomeric SNAP-GPI and higher degrees of oligomerization.

References

[1]   A. Fürstenberg and M. Heilemann. "Single-molecule localization microscopy — near-molecular spatial resolution in light microscopy with photoswitchable fluorophores". In: *Phys. Chem. Chem. Phys.* 15 (2013), pp. 14919–14930.

[2]   M. Sauer. "Localization microscopy coming of age: from concepts to biological impact". In: *Journal of Cell Science* 126 (2013), pp. 3505–3513.

[3]   F. Fricke et al. "One, two or three? Probing the stoichiometry of membrane proteins by single-molecule localization microscopy". In: *Scientific reports* 5 (2015).

[4]   T. Hallworth and M. G. Nichols. "The single molecule imaging approach to membrane protein stoichiometry". In: *Microscopy and Microanalysis* 18 (4 2012).

[5]   R. E. Thompson, D. R. Larson, and W. W. Webb. "Precise Nanometer Localization Analysis for Individual Fluorescent Probes". In: *Biophysical Journal* 82 (2002), pp. 2775–2783.

[6]   M. F. Garcia-Parajo et al. "Nanoclustering as a dominant feature of plasma membrane organization". In: *Journal of Cell Science* 127 (2014), pp. 4995–5005.

[7]   P. Annibale et al. "Photoactivatable Fluorescent Protein mEos2 Displays Repeated Photoactivation after a Long-Lived Dark State in the Red Photoconverted Form". In: *J Phys Chem Lett* (2010), pp. 1506–1510.

[8]   P. Annibale et al. "Quantitative photo activated localization microscopy: unraveling the effects of photoblinking". In: *PLoS ONE* 6 (2011), e22678.

[9]   P. Annibale et al. "Identification of clustering artifacts in photoactivated localization microscopy". In: *Nature methods* 8 (2011), pp. 527–528.

[10] S. L. Veatch et al. "Correlation functions quantify super-resolution images and estimate apparent clustering due to over-counting". In: *PLoS ONE* 7 (2012), e31457.

[11] P. Sengupta et al. "Probing protein heterogeneity in the plasma membrane using PALM and pair correlation analysis". In: *Nature Methods* 8 (2011), pp. 969–975.

[12] F. Baumgart et al. "Varying label density allows artifact-free analysis of membrane-protein nanoclusters". In: *Nature Methods* 13 (8 2016), pp. 661–664.

[13] F. B. Lopes et al. "Membrane nanoclusters of FcγRI segregate from inhibitory SIRPα upon activation of human macrophages". In: *Journal of Cell Biology* (jcb.201608094 2017).

[14] B. Alberts et al. *Molecular Biology of the Cell*. Garland Science, 2014.

[15] S. J. Singer and G. L. Nicolson. "The Fluid Mosaic Model of the Structure of Cell Membranes". In: *Science* 175 (4023 1972), pp. 720–731.

[16] D. M. Engelman. "Membranes are more mosaic than fluid". In: *Nature* 438 (7068 2005), pp. 578–580.

[17] S. K. Saka et al. "Multi-protein assemblies underlie the mesoscale organization of the plasma membrane". In: *Nature communications* 5 (2014), p. 4509.

[18] J. A. Torreno-Pina et al. "Enhanced receptor-clathrin interactions induced by N-glycan-mediated membrane micropatterning". In: *Proceedings of the National Academy of Sciences of the United States of America* 111 (2014), pp. 11037–11042.

[19] M. H. Ali and B. Imperiali. "Protein oligomerization: how and why". In: *Bioorg. Med. Chem.* 13 (2005), pp. 5013–5020.

[20] K. Hashimoto et al. "Caught in self-interaction: evolutionary and functional mechanisms of protein homooligomerization". In: *Phys. Biol.* 8 (2011), p. 035007.

[21] M. Lynch. "Evolutionary diversification of the multimeric states of proteins". In: *Proc. Natl. Acad. Sci. USA* 110 (30 2013), E2821–E2828.

[22] M. Cebecauer et al. "Signalling complexes and clusters: functional advantages and methodological hurdles". In: *J. Cell Sci.* 123 (2010), pp. 309–320.

[23] B. C. Lagerholm and N. L. Thompson. "Theory for ligand rebinding at cell membrane surfaces". In: *Biophys. J.* 74 (1998), pp. 1215–1228.

[24] K. A. K. Tanaka et al. "Membrane molecules mobile even after chemical fixation". In: *Nature methods* 7 (11 2010), pp. 865–866.

[25] S. Hennig et al. "Quantitative Super-Resolution Microscopy of Nanopipette-Deposited Fluorescent Patterns". In: *ACS Nano* 9 (2015), pp. 8122–8130.

[26] R. P. J. Nieuwenhuizen et al. "Quantitative localization microscopy: effects of photophysics and labeling stoichiometry". In: *PLoS ONE* 10 (5 2015), e0127989.

[27] B. D. Ripley. "Modelling spatial patterns". In: *J R Stat Soc Series B Stat Methodol* (1977), pp. 172–212.

[28] E. Betzig et al. "Near Field Scanning Optical Microscopy (NSOM): Development and Biophysical Applications". In: *Biophysical Journal* 49 (1 1986), pp. 269–279.

[29] S. W. Hell and J. Wichmann. "Breaking the diffraction resolution limit by stimulated emission: stimulated-emission-depletion fluorescence microscopy". In: *Optics Letters* 19 (11 1994), pp. 780–782.

[30] Thomas A. Klar and S. W. Hell. "Subdiffraction resolution in far-field fluorescence microscopy". In: *Optics Letters* 24 (14 1999), pp. 954–956.

[31] E. Betzig et al. "Imaging intracellular fluorescent proteins at nanometer resolution". In: *Science* 313 (5793 2006), pp. 1642–1645.

[32] M. J. Rust, M. Bates, and X. Zhuang. "Sub-diffraction-limit imaging by stochastic optical reconstruction microscopy (STORM)". In: *Nature Methods* 3 (10 2006), pp. 793–795.

[33] *Airy disk*. URL: `https://en.wikipedia.org/wiki/Airy_disk` (Last accessed: Mar. 2018).

[34] *Airy disk*. URL: `https://en.wikipedia.org/wiki/Angular_resolution` (Last accessed: Mar. 2018).

[35] S. van de Linde et al. "Direct stochastic optical reconstruction microscopy with standard fluorescent probes". In: *Nature protocols* 6 (2011), pp. 991–1009.

[36] M. Heilemann et al. "Subdiffraction-Resolution Fluorescence Imaging with Conventional Fluorescent Probes". In: *Angew. Chem. Int. Ed.* 47 (33 2008), pp. 6172–6176.

[37] S. T. Hess, T. P. K. Girirajan, and M. D. Mason. "Ultra-High Resolution Imaging by Fluorescence Photoactivation Localization Microscopy". In: *Biophysical Journal* 91 (11 2006), pp. 4258–4272.

[38] *Stokes shift*. URL: `https://commons.wikimedia.org/wiki/File:Stokes_shift.png` (Last accessed: Mar. 2018).

[39] O. Shimomura, F. H. Johnson, and Y. Saiga. "Extraction, purification and properties of aequorin, a bioluminescent protein from the luminous hydromedusan, Aequorea". In: *Journal of cellular and comparative physiology* 59 (3 1962), pp. 223–239.

[40] A. Small and S. Stahlheber. "Fluorophore localization algorithms for super-resolution microscopy". In: *Nature Methods* 11 (3 2014), pp. 267–279.

[41] C. S. Smith et al. "Fast, single-molecule localization that achieves theoretically minimum uncertainty". In: *Nature Methods* 7 (2010), pp. 373–375.

[42] A. van den Bos. *Parameter Estimation for Scientists and Engineers*. Wiley & Sons, 2007.

[43] P. Hinterdorfer and A. Van Oijen, eds. *Handbook of Single-Molecule Biophysics*. Springer, 2009.

[44] D. Axelrod, T. P. Burghardt, and N. L. Thompson. "Total Internal Reflection Fluorescence". In: *Annual Reviw of Biophysics and Bioengineering* 13 (1 1984), pp. 247–268.

[45] D. Axelrod. "Cell-substrate contacts illuminated by total internal reflection fluorescence". In: *The journal of cell biology* 89 (1 1981), pp. 141–145.

[46] K. N. Fish. "Total Internal Reflection Fluorescence (TIRF) Microscopy". In: *Current Protocols in Cytometry* 50 (1 2009), pp. 12.18.1–12.18.13.

[47] J. G. Donaldson. "Immunofluorescence Staining". In: *Curr. Protoc. Cell Biol.* 69 (2015).

[48] Evrogen. *Cyan-to-green photoswitchable fluorescent protein PS-CFP2*. URL: `http://evrogen.com/products/PS-CFP2/PS-CFP2_Detailed_description.shtml` (Last accessed: Mar. 2018).

[49] Thermo Fisher Scientific. *Alexa Fluor 647 dye*. URL: `https://www.thermofisher.com/us/en/home/life-science/cell-analysis/fluorophores/alexa-fluor-647.html` (Last accessed: Mar. 2018).

[50] Thermo Fisher Scientific. *Instructions TruboFect Transfection Reagent*. URL: `https://assets.thermofisher.com/TFS-Assets/LSG/manuals/MAN0011815_TurboFect_Transfection_Reag_UG.pdf` (Last accessed: Mar. 2018).

[51] Thermo Fisher Scientific. *Fluorescence SpectraViewer*. URL: `https://www.thermofisher.com/at/en/home/life-science/cell-analysis/labeling-chemistry/fluorescence-spectraviewer.html` (Last accessed: Mar. 2018).

[52] L. Nahidiazar et al. "Optimizing Imaging Conditions for Demanding Multi-Color Super Resolution Localization Microscopy". In: *PLoS ONE* 11 (7 2016), e0158884.

[53] M. Ovesny et al. "ThunderSTORM: a comprehensive ImageJ plug-in for PALM and STORM data analysis and super-resolution imaging". In: *Bioinformatics* 30 (16 2014), pp. 2389–2390.

[54] T. Wiegand and K. A. Moloney. *Handbook of Spatial Point-Pattern Analysis in Ecology*. CRC Press, Taylor & Francis Group, 2014.

[55] J. Illian et al. *Statistical Analysis and Modelling of Spatial Point Patterns*. John Wiley & Sons, Ltd., 2008.

[56] P. J. Diggle. *Statistical Analysis of Spatial and Spatio-Temporal Point Patterns*. CRC Press, Taylor & Francis Group, 2014.

[57] A. E. Gelfand et al., eds. *Handbook of Spatial Statistics*. CRC Press, Taylor & Francis Group, 2010.

[58] H. W. Lotwick and B. W. Silverman. "Methods for Analysing Spatial Processes of Several Types of Points". In: *J. R. Statis. Soc.* 44 (1982), pp. 406–413.

[59] P. Grabarnik, M. Myllymäki, and D. Stoyan. "Correct testing of mark independence for marked point patterns". In: *Ecological Modelling* 222 (23 2011), pp. 3888–3894.

[60] N. B. Loosmore and E. D. Ford. "Statistical inference using the G or K point pattern spatial statistics". In: *Ecology* 87 (8 2006), pp. 1925–1931.

Appendix A

Parameters

A.1   Simulation Parameters

Variable	Value	
$\mu_{p.a.}$	30	Mean of p.a.
$\sigma_{p.a.}$	10	Standard deviation of p.a.
l_{low}	10	Lower bound of p.a.
l_{up}	50	Upper bound of p.a.

Table A.1: Localization precision. Parameters for the distribution of positional accuracy given in nm.

Variable	Value 1	Value 2	Value 3	
a	10000	10000	10000	Region of interest
N_{mols}	100	100	100	Number of molecules per μm^2
ζ	0	0.7	0.8	Monomer fraction
η	0.95	0.6	0.4	Labeling efficiency
α	0.5	0.5	0.3	Label ratio
N_{bg}	10	20	20	Number background loc. per μm^2
$N_{\mathrm{ub,A}}$	5	10	10	Number unspecifically bound labels A per μm^2
$N_{\mathrm{ub,B}}$	5	10	10	Number unspecifically bound labels B per μm^2
c_{blink}	KT3	KT3	KT3	Blinking statistics (for labels A and B)
N_{frames}	10000	10000	10000	Number of recorded frames

Table A.2: Parameters for simulations of oligomers (parameter sets 1, 2 and 3).

Simulation	$c_{\text{blink,A}}$	$c_{\text{blink,B}}$	N_{mols}	η	α	N_{bg}	$N_{\text{ub,A}}$	$N_{\text{ub,B}}$
1	Alexa647-KT3	Alexa647-KT3	100	0.95	0.5	10	5	5
2	Alexa647-KT3	PS-CFP2	100	0.95	0.5	10	5	5
3	PS-CFP2	Alexa647-KT3	100	0.95	0.5	10	5	5
4	Alexa647-KT3	Alexa647-H57	100	0.95	0.5	10	5	5
5	Alexa647-H57	Alexa647-KT3	100	0.95	0.5	10	5	5
6	PS-CFP2	Alexa647-H57	100	0.95	0.5	10	5	5
7	Alexa647-H57	PS-CFP2	100	0.95	0.5	10	5	5
8	Alexa647-KT3	Alexa647-KT3	50	0.95	0.5	10	5	5
9	Alexa647-KT3	Alexa647-KT3	150	0.95	0.5	10	5	5
10	Alexa647-KT3	Alexa647-KT3	100	0.4	0.5	10	5	5
11	Alexa647-KT3	Alexa647-KT3	100	0.95	0.2	10	5	5
12	Alexa647-KT3	Alexa647-KT3	100	0.95	0.8	10	5	5
13	Alexa647-KT3	Alexa647-KT3	100	0.95	0.5	50	5	5
14	Alexa647-KT3	Alexa647-KT3	100	0.95	0.5	100	5	5
15	Alexa647-KT3	Alexa647-KT3	100	0.95	0.5	10	20	20
16	Alexa647-KT3	Alexa647-KT3	100	0.95	0.5	10	50	50
17	PS-CFP2	Alexa647-KT3	100	0.95	0.8	100	50	50
18	PS-CFP2	Alexa647-KT3	100	0.4	0.8	100	50	50

Table A.3: Parameters for simulations of random molecule distributions.
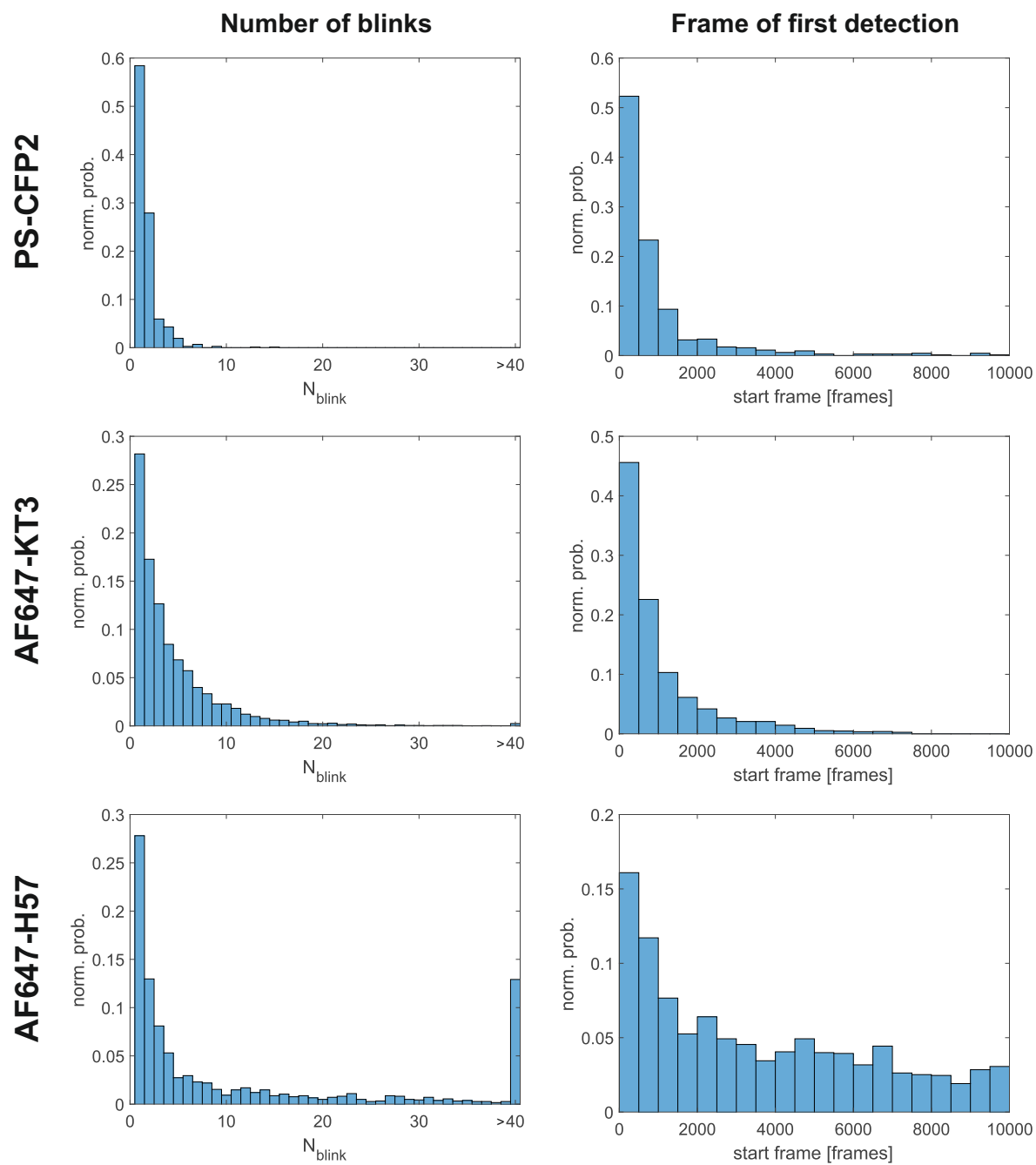
A.2 Blinking Statistics

Figure A.1: Blinking statistics. Number of blinks and frame number of first detection given as normalized histograms for PS-CFP2, Alexa647-KT3 and Alexa647-H57. Data recorded and analyzed by Benedikt Rossboth and Florian Baumgart.
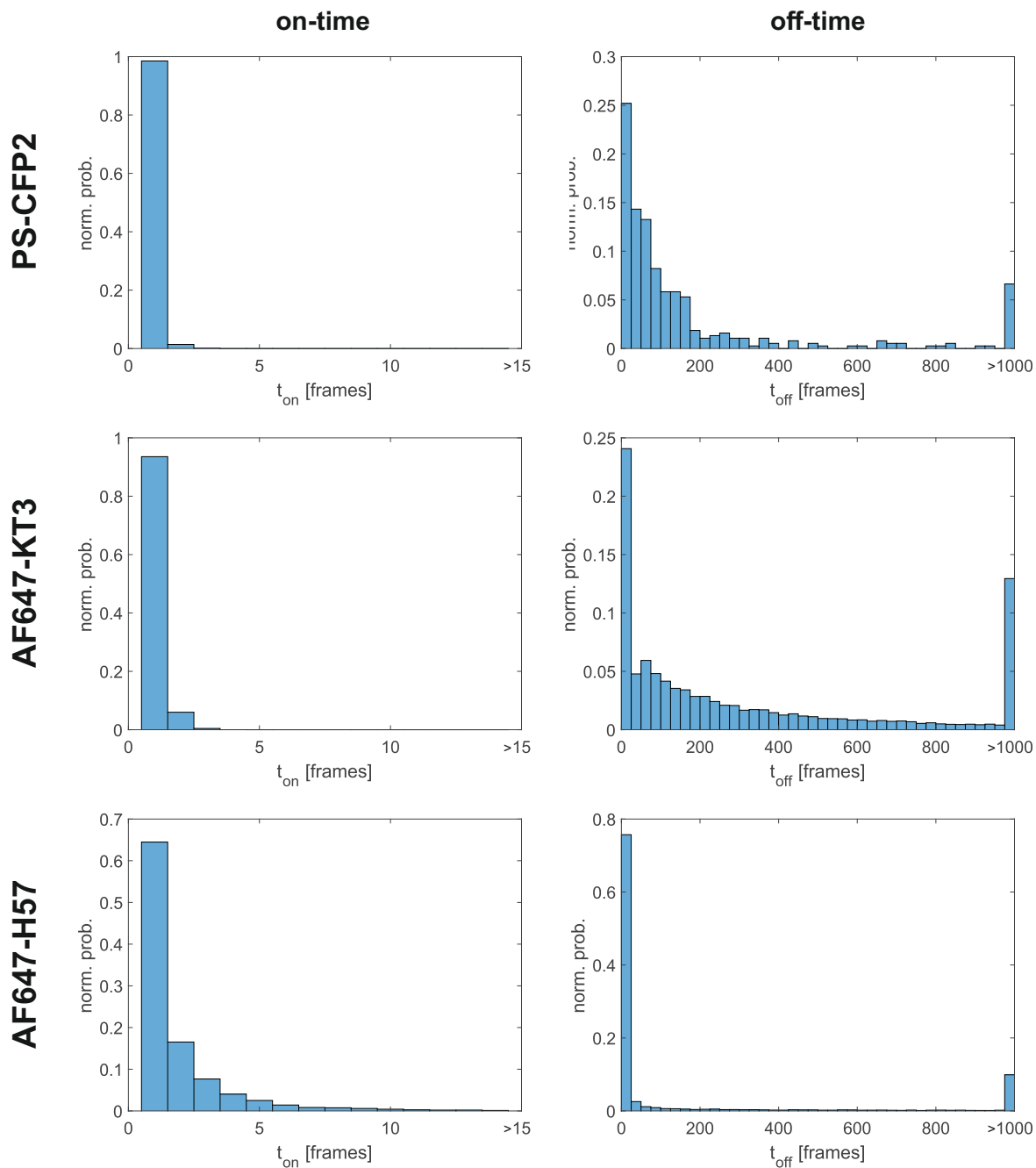
Figure A.2: Blinking statistics. Number of consecutive frames that a fluorophore is in the bright state (on-time) and dark state (off-time) given as normalized histograms for PS-CFP2, Alexa647-KT3 and Alexa647-H57. Data recorded and analyzed by Benedikt Rossboth and Florian Baumgart.

A.3   Parameters for ThunderSTORM analysis

Camera setup

Pixel size [nm]	100.0
Photoelectrons per A/D count	16.5
Base level [A/D counts]	100.0
EM gain	300.0

Image filtering

Filter	Wavelet filter (B-Spline)
B-Spline order	3
B-Spline scale	2.0

Approximate localization of molecules

Method	Local maximum
Pixel intensity threshold (Channel 1)	1.6*std(Wave.F1)
Pixel intensity threshold (Channel 2)	2.0*std(Wave.F1)
Connectivity	8-neighbourhood

Sub-pixel localization of molecules

Method	PSF: Integrated Gaussian
Fitting radius [px]	4
Fitting method	Maximum likelihood
Initial sigma [px]	1.6
Multi-emitter fitting analysis	disabled

Post-processing filters

Intensity	intensity > 50
Uncertainty	med(uncert.) - 0.6*med(uncert.) < uncert. < med(uncert.) + 1.4*med(uncert.)
Sigma	0.6*med(sigma) < sigma < 1.4*med(sigma)